

# TIMBER v0.1: a conceptual framework for emulating temperature responses to tree cover change

Shruti Nath<sup>1,2</sup>, Lukas Gudmundsson<sup>2</sup>, Jonas Schwaab<sup>2</sup>, Gregory Duveiller<sup>3</sup>, Steven J. De Hertog<sup>4</sup>, Suqi Guo<sup>5</sup>, Felix Havermann<sup>5</sup>, Fei Luo<sup>6,7</sup>, Iris Manola<sup>6</sup>, Julia Pongratz<sup>5,8</sup>, Sonia I. Seneviratne<sup>2</sup>, Carl F. Schleussner<sup>1,9</sup>, Wim Thiery<sup>4</sup>, and Quentin Lejeune<sup>1</sup>

<sup>1</sup>Climate Analytics, Berlin, Germany

<sup>2</sup>Institute of Atmospheric and Climate Science, ETH Zurich, Zurich, Switzerland

<sup>3</sup>Department of Biogeochemical Integration, Max Planck Institute for Biogeochemistry, Jena, Germany

<sup>4</sup>Vrije Universiteit Brussel, Department of Hydrology and Hydraulic Engineering, Brussels, Belgium

<sup>5</sup>Ludwig-Maximilians-University Munich, Department of Geography, Munich, Germany

<sup>6</sup>Vrije Universiteit Amsterdam, Institute for Environmental studies, Amsterdam, Netherlands

<sup>7</sup>Royal Netherlands Meteorological Institute (KNMI), De Bilt, Netherlands

<sup>8</sup>Max Planck Institute for Meteorology, Hamburg, Germany

<sup>9</sup>Integrative Research Institute on Transformations of Human-Environment Systems (IRI THESys) and Geography Department, Humboldt-Universität zu Berlin, Berlin, Germany

**Correspondence:** shruti.nath@climateanalytics.org

**Abstract.** Land cover changes have been proposed to play a significant role, alongside emission reductions, towards achieving the temperature goals agreed upon under the Paris Agreement. Such changes carry both global implications, pertaining to the biogeochemical effects of land cover change and thus the global carbon budget, and regional/local implications, pertaining to the biogeophysical effects arising within the immediate area of land cover change. Biogeophysical effects of land cover change are of high relevance to national policy- and decision- makers and accounting for them is essential towards effective deployment of land cover practices that optimises between global and regional impacts. To this end, Earth System Model (ESM) outputs that isolate the biogeophysical responses of climate to land cover changes are key in informing impact assessments and supporting scenario development exercises. However, generating multiple such ESM outputs in a manner that allows comprehensive exploration of all plausible land cover scenarios is computationally untenable. This study proposes a framework to explore in an agile manner the local biogeophysical responses of climate under customised tree cover change scenarios by means of a computationally inexpensive emulator, TIMBER v0.1. The emulator is novel in that it solely represents the biogeophysical responses of climate to tree cover changes, and can be used as either a standalone device or supplementary to existing climate model emulators that represent the climate responses from greenhouse gas (GHG) or Global Mean Temperature (GMT) forcings. We start off by modelling local minimum, mean and maximum surface temperature responses to tree cover changes by means of a month- and Earth System Model (ESM)- specific Generalised Additive Model (GAM) trained over the whole globe. 2-m air temperature responses are then diagnosed from the modelled minimum and maximum surface temperature responses using observationally derived relationships. Such a two-step procedure accounts for the different physical representations of surface temperature responses to tree cover changes under different ESMs, whilst respecting a definition of 2-m air temperature that is more consistent across ESMs and with observational datasets. In exploring new tree cover

20 change scenarios, we employ a parametric bootstrap sampling method to generate multiple possible temperature responses,  
such that the parametric uncertainty within the GAM is also quantified. The output of the final emulator is demonstrated for  
the SSP 1-2.6 and 3-7.0 scenarios. Relevant temperature responses are identified as those displaying a clear signal in relation  
to their surrounding parametric uncertainty, calculated as the "signal-to-noise" ratio between the sample set mean and sample  
set variability. The emulator framework developed in this study thus provides a first step towards bridging the information-gap  
25 surrounding biogeophysical implications of land cover changes, allowing for smarter land-use decision making.

## 1 Introduction

Following the Paris Agreement in 2015, 42% of Nationally Determined Contributions (NDCs) submitted by countries included  
afforestation/reforestation based actions and targets (Seddon et al., 2020). The recent COP26 in Glasgow furthermore saw a  
pledge to halt and reverse deforestation by 2030 (COP, 2021). Considering this, society is set to experience notable land cover  
30 changes in hopes to achieve global warming levels well below +2 °C and pursue efforts in limiting them to +1.5 °C above pre-  
industrial levels. In anticipation of this, the Earth System Model (ESM) community has put great effort into understanding and  
quantifying the biogeochemical and biogeophysical effects of land cover changes (De Noblet-Ducoudré et al., 2012; Lawrence  
et al., 2016; Davin et al., 2020; Boysen et al., 2020).

Biogeochemical effects of land cover changes largely affect the global carbon budget, while biogeophysical effects are essen-  
35 tial towards understanding regional climate impacts as well as extremes (De Noblet-Ducoudré et al., 2012; Pitman et al., 2012;  
Lejeune et al., 2018). Recent studies by Windisch et al. (2021) and Lawrence et al. (2022), highlighted the need to consider the  
biogeophysical effects of land cover changes in order to effectively identify and prioritise areas for re/afforestation and con-  
servation. Such underscores the regional importance of the biogeophysical effects of land cover changes under future climate  
scenarios (Seneviratne et al., 2018; Hirsch et al., 2018), and evidences the need to consider them within impact assessments  
40 (Popp et al., 2017) and scenario development exercises (Van Vuuren et al., 2012; Calvin and Bond-Lamberty, 2018). Exploring  
the biogeophysical effects of land cover changes under all possible future land cover scenarios solely through ESMs however,  
quickly becomes untenable due to computational costs, and it is worth pursuing computationally inexpensive alternatives such  
as climate model emulators.

Climate model emulators are computationally inexpensive tools, trained on available climate model runs to then render  
45 probability distributions of key climate variables for runs that have not been generated yet. By statistically representing select  
climate variables, emulators are able to reduce the dimensionality of climate model outputs, allowing for agile exploration of the  
uncertainty phase space surrounding climate projections. Climate model emulators designed to reproduce regional/grid point  
level, annual to monthly temperature projections usually operate as ESM-specific and start by deterministically representing  
the regional/grid point level mean response of temperatures to a certain forcing, after which the residual variability – treated as  
50 the uncertainty due to natural climate variability – is sampled or stochastically generated (Alexeeff et al., 2018; McKinnon and  
Deser, 2018; Link et al., 2019; Castruccio et al., 2019; Beusch et al., 2020; Nath et al., 2022b). Outputs of such emulators act  
as approximations of multi-model initial-condition ensembles, providing distributions of temperature responses to the forcing

of choice for impact assessments. To date however, such climate model emulators mainly represent the greenhouse gas (GHG)- or Global Mean Temperature (GMT)- forcing within their mean response, neglecting the biogeophysical effects of land cover changes.

In this study, we set up a conceptual framework for emulating the biogeophysical responses of climate variables to land cover changes, hereafter referred to simply as "responses". As a first step, we focus on emulating the surface and 2-m air temperature responses to land cover changes between forest and cropland, simply denoted as "tree cover changes". The resulting emulator constitutes a prototype version of the Tree cover change cLIimate Biophysical responses EmulatoR, i.e. TIMBER v0.1. Since representation of natural climate variability is well-explored in other emulators, TIMBER v0.1 purely focusses on representing the mean response of temperatures to tree cover change. In doing so, we recognise that the ESM data available for training (described under Section 2) is under-representative of the full range of possible tree cover changes across the globe. Consequently, we pursue a more probabilistic representation, such that parametric uncertainties given the training data population are accounted for. TIMBER v0.1 can thus be used as a standalone device or as supplementary to other emulators. The structure of this paper is as follows: Section 3 introduces the emulator framework and its calibration and evaluation procedure; Section 4 presents the calibration and evaluation results, and illustrates some emulator outputs; Section 4.4 demonstrates the application of the emulator to different Shared Socio-economic Pathway (SSPs) scenarios; and Section 5 wraps up with the conclusion and outlook.

## 2 Data

### 2.1 ESM experiments

Idealised Earth System Model (ESM) experiments that isolate the effects of tree cover change on the climate were run as part of the LAnd MAnagement for CLimate Mitigation and Adaptation (LAMA CLIMA) project, a detailed description of these simulations can be found in (De Hertog et al., 2022). The experimental setup was designed to capture the maximal potential climate response due to af/re/deforestation as compared to present-day land cover conditions. Accordingly, extreme afforestation (AFF) and deforestation (DEF) scenarios were run alongside a reference scenario (REF). The REF scenario spans 150 years with land cover conditions and other forcings (GHG emissions etc.) kept constant at 2015 levels. The AFF (DEF) scenario then consists of full expansion of forest (crop) cover relative to that of 2015 levels with all other forcings again kept constant at 2015 levels, and again span 160 years with a 10 year spin up period which is excluded. The AFF (DEF) was implemented by removing the non required vegetation types (i.e. crops, grassland and shrubs for AFF and forest, grasslands and shrubs for DEF) and upscaling the remaining vegetation to fill up the grid cells. Bare land was conserved throughout this process in order to respect the biophysical limits of where vegetation can grow. The difference between AFF (DEF) run and REF run outputs averaged over the 150 years provides the climate response to idealised re/afforestation (deforestation).

Temperature responses derived from the ESM simulations are distinguished into local and non-local responses following the checkerboard approach developed by Winckler et al. (2017c). Local responses represent the expected climate responses to

85 land cover change within the immediate area of change and can be applied in any global tree cover change scenario, whereas non-local responses represent remote effects of land cover change and depend on the global extent and patterns of land cover change. Given that local responses are independent of the global extent and patterns of land cover change, we focus only on them for the rest of this study and the term "response" exclusively refers to the local response hereon. Participating ESMs running simulations within the LAMACLIMA project are the Community Earth System Model version 2.1.3 (CESM2), the  
90 Max Planck Institute Earth System Model version 1.2 (MPI-ESM) and the European Community Earth System Model version 3-Veg (EC-EARTH).

## 2.2 Observational dataset

To demonstrate the applicability of the emulating approach outlined in this study on observational data we use the Duveiller et al. (2018c) dataset, hereafter referred to as D18. This dataset was derived using a "space-for-time" substitution approach  
95 applied on surface temperatures from satellite data, in order to map potential local responses of daytime, mean and nighttime surface temperatures to land cover transitions. It considers transitions from forest to several other land cover types (e.g. shrubland, grassland etc.). To ensure comparability with the ESM runs, we choose to only focus on forest transitions to cropland, which are hereafter by analogy also referred to as DEF. It should be noted that we don't emulate the temperature response to afforestation in this case since the D18 dataset assumes a symmetrical temperature response for transitions from cropland  
100 to forests. Additionally, the dataset contains some information gaps in space and is thus spatially sparse as compared to the spatially complete ESM output fields.

## 2.3 Tree cover change scenarios in selected SSPs

The emulator framework developed in this study enables to predict the expected local temperature changes that would be given by the dataset it is trained on (being derived from models or observations) in response to any scenario of spatially explicit tree  
105 cover changes. We apply it to scenarios of tree cover changes according to the Shared Socioeconomic Pathways SSP1-2.6 and SSP3-7.0 (Riahi et al., 2017).

SSP1-2.6 follows the narrative of a global trend towards sustainable development from SSP1 (Riahi et al., 2017), and entails changes in global emissions and further climate forcings that eventually lead to a radiative forcing of  $2.6 \text{ W/m}^2$  in 2100. Strong land-use regulations mean that tropical deforestation is reduced, while economic development enables increases in crop yields  
110 and the focus on sustainability entails less food waste and a reduction in consumption of animal products (Popp et al., 2017). Overall, this leads to an increase in forest cover in many parts of the world. In contrast, SSP3-7.0 follows the SSP3 narrative and leads to a radiative forcing of  $7.0 \text{ W/m}^2$  in 2100. SSP3 features a world in which there is a resurgence of nationalism and regional conflicts that translates into a stronger focus on domestic and regional issues and low international cooperation in particular on environmental issues. Land use is thus not well regulated, low economic development and reduced technology  
115 transfer mean that crop yields stagnate or decline, while diets with high shares of animal products and high rates of food waste prevail. As a result, deforestation continues especially in the tropics.

In this study, we use the trajectories of tree cover changes according to these two scenarios as modelled by the Integrated Assessment Models, IMAGE and MESSAGE-GLOBIOM (van Vuuren et al., 2017; Fujimori et al., 2017). Tree fraction maps are obtained as the CMIP6 variable "treeFrac", from the CMIP6 new generation library hosted by ETH Zürich (Brunner et al., 120 2020).

## 3 Methods

### 3.1 Overview of the emulation approach

The emulation framework presented in this study aims at predicting local temperature responses to tree cover changes, and is split into three parts. The first part seeks to statistically represent the expected responses of minimum ( $\Delta T S_{m,s}^{min}$ ), mean 125 ( $\Delta T S_{m,s}^{mean}$ ) and maximum ( $\Delta T S_{m,s}^{max}$ ) surface temperature for a given month  $m$  and location  $s$ , generically referred to as  $\Delta T S_{m,s}$ , to tree cover change (Sect. 3.2). This is carried out using a Generalized Additive Model (GAM) that is calibrated via a blocked cross validation procedure in order to account for the specificity of the training data. The predictive ability of the GAM is also evaluated using a blocked cross-validation procedure.

The second part then seeks to diagnose 2-m air temperature responses ( $\Delta T_{m,s}^{2m}$ ) from the statistically represented surface 130 temperature responses using observationally derived relationships (Sect. 3.3).  $T_{m,s}^{2m}$  is an important variable for impact assessments, however is diagnosed differently across ESMs (leading to inter-ESM discrepancies in their modelled response to tree cover change) and is also defined differently between ESMs and observations. The split approach suggested in this study therefore allows to maintain a response of surface temperature to tree cover change that is specific to the ESM/observational data trained on, from which  $\Delta T_{m,s}^{2m}$  is then diagnosed using observationally derived relationships independent of training data. In 135 such, we account for the different physical representations of temperature responses to tree cover change for each ESM, whilst also ensuring a consistent definition of  $\Delta T_{m,s}^{2m}$  across ESMs and with observational datasets, ergo the possibility to compare them.

The third part aims to quantify the uncertainty in the final  $\Delta T_{m,s}^{2m}$  predictions, that arise from the parametric uncertainties within the GAM (Section 3.4). The GAM's parametric uncertainty is assessed using a parametric bootstrap procedure (Hastie 140 and Tibshirani, 1986; Wood, 2017), so as to evaluate the imperfections within its fitted parameters conditional on the given training sample population. Given the limited amount of training data available, this is an important step towards quantifying the confidence in the temperature response predictions from TIMBER.

### 3.2 Representing the expected surface temperature responses to tree cover change

In the following subsections, we introduce the statistical model used for representing  $\Delta T S_{m,s}$  to tree cover changes (Section 145 3.2.1), followed by our approach in calibrating (Section 3.2.2) and evaluating it (Section 3.2.3). In choosing and calibrating the model, we are especially mindful of the training datasets being solely representative of grid points which undergo both directions of extreme tree cover changes relative to the REF scenario, as performed within the ESM training simulations, or

just one direction (i.e. deforestation) in the case of the D18 data. Consequently, we require a model that can train over the whole globe (as otherwise there are at most two samples per grid point to train on) and need to account for the resulting spatially-structured training data during model calibration. To this end, a random train/test split cannot be applied during model calibration due to the structural interdependencies in the ESM and observational data (for example arising through spatial correlations). We therefore calibrate the model following a blocked cross validation procedure (Roberts et al., 2017). Moreover, we recognise that evaluation can only be done on the training datasets as no other ESM simulations isolating the local effects from af- or deforestation with the checkerboard approach of Winckler et al. (2017a) exist, and thus settle for synthesising the best representation of the model’s out-of-sample performance during model evaluation, by again employing blocked cross-validation.

### 3.2.1 Model description

We model the expected  $\Delta TS_{m,s}$  conditional on tree cover change and geographical attributes using a month-specific Generalized Additive Model (GAM) trained over the whole globe. The GAM, hereon referred to as  $\Gamma_m^{\min/mean/max}$  – depending on whether it is applied to daily minimum, maximum or mean surface temperature – or more generically as  $\Gamma_m$ , is provided by the python pyGAM package.  $\Gamma_m$  can easily ingest multidimensional data and has the advantage that it does not prescribe any functional form, allowing flexibility in representing linear to more complex response types. The input predictor matrix ( $\mathbf{X}$ ) given to  $\Gamma_m$  is composed of tree cover changes relative to the 2015 ( $\Delta_{2015}treeFrac$ ) and geographical attributes of longitude ( $lon$ ), latitude ( $lat$ ) and orography ( $orog$ ). Maps of  $\Delta_{2015}treeFrac$  implemented under the AFF and DEF scenarios, and the  $orog$  (defined as meters above sea level) are available for reference in Figures A1 and A2 respectively, Appendix A. The conditional distribution of  $\Delta TS_{m,s}$  is assumed as normal,

$$\Gamma_m = \mathbb{E}[\Delta TS_{m,s} | \mathbf{X}] = te_m(\Delta_{2015}treeFrac_{m,s}, lon_s, lat_s, by = orog_s) \quad \text{where} \quad [\Delta TS_{m,s} | \mathbf{X}] \sim \mathcal{N} \quad (1)$$

$te_m$  represents a tensor spline term built across the three-dimensional  $\Delta_{2015}treeFrac, lon, lat$  space with coefficient terms stratified according to  $orog$  using the  $by$  operator so as to create a varying coefficient model (Hastie and Tibshirani, 1993). For further details on tensor splines and the  $by$  operator, see Wood (2017).  $\Gamma_m$  can be calibrated for its lambda parameter ( $\lambda$ ), which controls the complexity in shape of  $te_m$  (where a smaller  $\lambda$  value allows for a more complex shape) and its number of basis functions, also noted  $nbf$  (where more basis functions means more degrees of freedom).

### 3.2.2 Blocked cross validation for model calibration

A first blocked cross validation ((Roberts et al., 2017)) is conducted to find the model configuration, (i.e., the set of model parameters  $\lambda$  and  $nbf$ ) that performs best over geographical and climate regions (Steps 1-4 of Figure 1). Block samples are constructed by identifying regions sharing climate and geographical characteristics. K-means clustering is used to cluster grid points according to background climate (based on climatological values of temperature and relative humidity) in the REF simulation of each ESM and in historical climatological data from WorldClim v2 (<https://www.worldclim.org/data/worldclim21>).

html) when further calibrating on the D18 observational data. To select the optimal number of clusters, we calculate the im-  
180 provement in performance of the K-means clustering algorithm (measured as the average distance of all points from the centre  
of their respective cluster groups, a smaller distance indicating better performance) with increasing number of clusters, then  
select the number of clusters after which no further improvement in performance is observed. Grid points are subsequently split  
according to continuous geographical regions: Africa, North America, South America, Australia, Eurasia, Tibetan Plateau and  
the South-East Asian Islands. The composite cluster blocks obtained through this procedure are illustrated on the upper-right  
185 corner of Figure 1 (for example ESM, CESM2) and on Figure A1.

Cross validation is then performed using the composite blocks identified in both the climate and geographical space. Suc-  
cessively and for each block,  $\Gamma_m$  is fitted on data for the whole land area except over that block. At each iteration,  $\lambda$  values  
between 0.001 and 1 as well as a number of basis functions between 5 and 9 are tried out, representing a possible model  
configuration. For each block, the performance of each model configuration is evaluated by calculating the RMSEs its predic-  
190 tions and the actual ESM or observational data over that block. By doing so, we hope to nudge the  $\lambda$  parameter and number  
of basis functions to values that most flexibly apply across all possible geographical and climate conditions whilst ensuring  
independence between training and test sets by accounting for spatial correlations. Eventually, cross validation is carried out  
across all train-test splits such that each block is used for testing once, and the set of model parameters yielding the best per-  
formance for  $\Gamma_m$  as measured by the RMSE across all test sets is selected. The parameters of these model configurations and  
195 their performance are shown in Section 4.1.1.

### 3.2.3 Blocked cross validations for model evaluation

Having selected the optimal  $\lambda$  value and nbf configuration for  $\Gamma_m$ , a final training on the whole set of training data is  
conducted to obtain the fully calibrated  $\Gamma_m$ . Blocked cross validation is further employed to evaluate the calibrated  $\Gamma_m$ 's  
performance into "no-analogue" conditions where the model has the least information (Roberts et al., 2017), thus providing  
200 a representative idea of the model's ability to predict into new tree cover change scenarios unseen during calibration. It is  
mainly required that the model is able to predict well across different background climates as well as for different amounts of  
tree cover change, therefore its performance is evaluated separately in no-analogue conditions representative of each of these  
aspects.

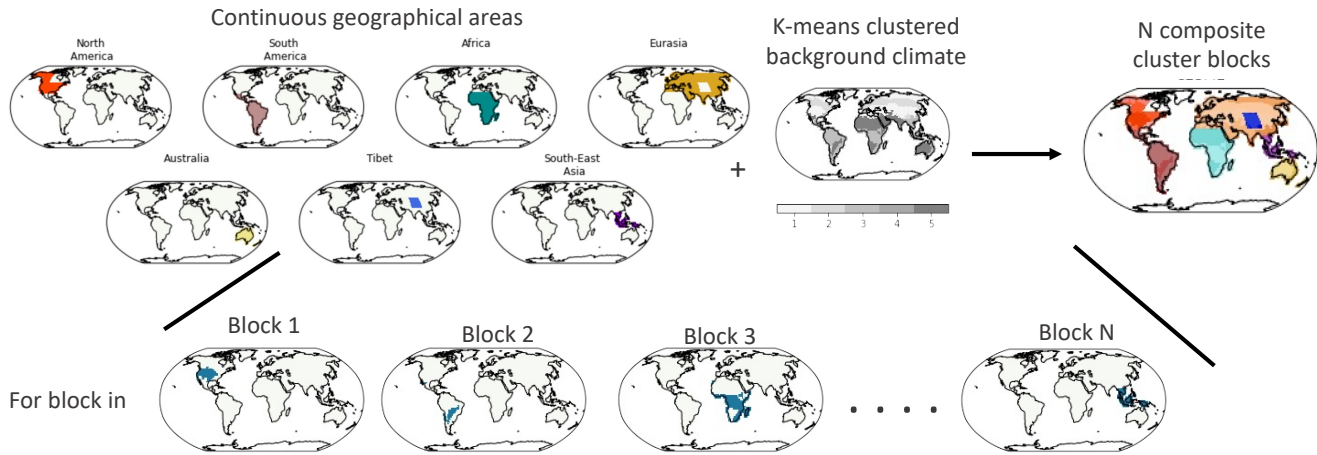
First, since  $\Gamma_m$  was originally calibrated by creating blocks that considered both climate and geographical space, the perfor-  
205 mance into "no-analogue" background climates is assessed by re-using those same blocks. Successively and for each block, the  
best performing configuration of  $\Gamma_m$  identified during calibration is trained on data for the whole land area except that block.  
The RMSEs between the values predicted by  $\Gamma_m$  and the actual values in the ESM or observational data over that block are  
then calculated. The results of this procedure are described in Section 4.1.2.

Then, another set of blocks is constructed by splitting the same seven continuous geographical regions as in the previous sec-  
210 tion, but by dividing the grid cells constituting those according to the amount of tree cover change  $\Delta_{2015}treeFrac$  encountered  
between the REF and AFF or REF and DEF simulations, using bins of  $\Delta_{2015}treeFrac$  magnitudes: [0.01-0.15), [0.15-0.3),  
[0.3-0.5), [0.5-0.8) and [0.8-1.0], for both positive and negative signs of tree cover change. A similar procedure to that applied

for the no-analogue background climate conditions is then conducted but using these newly constructed blocks: Successively and for each block,  $\Gamma_m$  is trained on data for the whole land area except over that block, using the sets of parameters identified in Section 3.2.2. For each block, the RMSEs between the values predicted by  $\Gamma_m$  and the actual ESM or observational data are then calculated. They constitute an estimate of the predictive ability of  $\Gamma_m$  for tree cover change amounts unseen during training and are presented in Section 4.1.3.

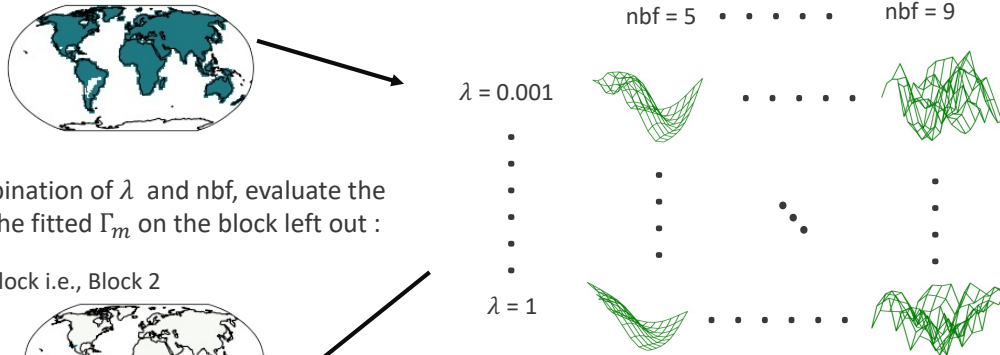


1. Identify continuous geographical regions sharing similar climate conditions



2. Fit  $\Gamma_m$  on data for the whole land area except the block by trying out all combinations of  $\lambda$  and nbf :

E.g. training material for  $\Gamma_m$  tested on Block 2

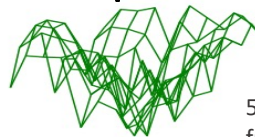


3. For each combination of  $\lambda$  and nbf, evaluate the performance of the fitted  $\Gamma_m$  on the block left out :

E.g. Test block i.e., Block 2



4. Identify the best performing  $\lambda$  and nbf combination by considering RMSEs across all test blocks



5. Evaluate the predictive ability of the fully calibrated  $\Gamma_m$  using another round of blocked cross-validation

**Figure 1.** Framework for block cross validation used for the calibration and the evaluation of  $\Gamma_m$ , based on its ability to predict the surface temperature response to tree cover changes over climate and continuous geographical regions not considered during model calibration.

### 3.3 Diagnosing the 2-m air temperature response from changes in surface temperatures

Hooker et al. (2018) were able to derive month-specific relationships between observational night and day surface temperatures ( $TS_{m,s}^{night/day}$ ) and observational  $T_{m,s}^{2m}$  (provided by the Global Historical Climatology Network monthly (Menne et al., 2018)). They did so by performing both Geographical and Climate Space Weighted Regression (GWR and CSWR) between observational  $TS_{m,s}^{night/day}$  and observational  $T_{m,s}^{2m}$  values, so as to obtain grid point level coefficients specific to geographical/background climate conditions. By taking a stacked generalisation of the GWR and CSWR outputs, Hooker et al. (2018) were able to reconstruct global  $T_{m,s}^{2m}$  maps over the period 2003 to 2016 in a geographically and climatically consistent manner.

In this study, we use the Hooker et al. (2018) model to diagnose  $T_{m,s}^{2m}$  from surface temperatures. Ideally, the Hooker et al. (2018) model would be refitted to derive ESM-specific coefficients between ESM surface temperatures and observed  $T_{m,s}^{2m}$  data. Given that this study primarily focusses on setting up a conceptual framework however, we choose to directly apply the original coefficients derived by Hooker et al. (2018) as an initial proof-of-concept. Before applying the Hooker et al. (2018) model, we first make some modifications to it so as to enable a smooth translation between observed and ESM spaces. In the following subsections, we introduce the modifications made to the Hooker et al. (2018) model and furthermore outline some tests performed to check that the modified version of it applied to ESMs still yields results comparable to those expected from observations.

#### 3.3.1 Modifications of the Hooker et al. (2018) model

$T_{m,s}^{2m}$  values are diagnosed using a modified version of the Hooker et al. (2018) model which uses  $TS_{m,s}^{min/max}$  values instead of  $TS_{m,s}^{night/day}$  and only considers the GWR coefficient terms,

$$T_{m,s}^{2m} = \beta_{0,m,s}^{GWR} + \beta_{1,m,s}^{GWR} \cdot TS_{m,s}^{min} + \beta_{2,m,s}^{GWR} \cdot TS_{m,s}^{max} \quad (2)$$

assuming that the effects of land cover type are minimal on  $\beta_{0,m,s}^{GWR}$ , we then get,

$$\Delta T_{m,s}^{2m} = \beta_{1,m,s}^{GWR} \cdot \Delta TS_{m,s}^{min} + \beta_{2,m,s}^{GWR} \cdot \Delta TS_{m,s}^{max} \quad (3)$$

Where  $\beta_{0,m,s}^{GWR}$ ,  $\beta_{1,m,s}^{GWR}$  and  $\beta_{2,m,s}^{GWR}$  are coefficient terms obtained from GWR. We choose not to use the CSWR coefficient terms as background climates between observations and ESMs are not consistent and there is the additional uncertainty surrounding the evolution of CSWR coefficient terms under changing background climates. Additionally, we use  $TS_{m,s}^{min/max}$  values instead as they are the only available DEF and AFF scenario ESM outputs which are most similar to  $TS_{m,s}^{night/day}$ .

#### 3.3.2 Tests on the modified Hooker et al. (2018) model applied to the ESM space

Since we look at relative changes in  $T_{m,s}^{2m}$ , the modifications made to the Hooker et al. (2018) model are expected to have minimal impact as long as the biases in  $T_{m,s}^{2m}$  values calculated using ESM  $TS_{m,s}^{min/max}$  values have the same spread as those

arising from natural variability within observational  $TS_{m,s}^{night/day}$  values, and are thus "acceptable". To determine this, we compare the spread of biases obtained when calculating  $T_{m,s}^{2m}$  values from observational  $TS_{m,s}^{night/day}$  values to those obtained from  $TS_{m,s}^{min/max}$  ESM outputs for the REF scenario.  $TS_{m,s}^{min/max}$  outputs from the REF scenario are used, as we consider them representative of the natural variability surrounding  $TS_{m,s}^{min/max}$  values. We approximate the spread of biases by taking  
 250 into account the natural variability surrounding the surface temperature values and compare them through the following steps:

1. Construct a multivariate Gaussian process across all observational  $TS_{m,s}^{night/day}$  values to generate spatially correlated pairs of  $TS_{m,s}^{night/day}$  which also take into account cross-correlations between  $TS_{m,s}^{night}$  and  $TS_{m,s}^{day}$ . Generated  $TS_{m,s}^{night/day}$  pairs will act as "pseudo-samples" that represent the underlying uncertainty due to natural variability within observational data.
- 255 2. For each timestep of  $T_{m,s}^{2m}$  predictions available from the original Hooker et al. (2018) model (going from 2003 to 2016):
  - (a) Generate 100 synthetic pairs of  $TS_{m,s}^{night/day}$  values using the Gaussian process constructed in Step 1.
  - (b) Calculate the biases between the  $T_{m,s}^{2m}$  prediction available from the original Hooker et al. (2018) model and those obtained by applying Equation 2 to the synthetically generated pairs of  $TS_{m,s}^{night/day}$ .
3. Take the [<sup>1</sup>] Interquartile Range (IQR) of the biases calculated in Step (2b) as a measure of their spread.
- 260 4. Repeat steps 1-3 for  $TS_{m,s}^{min/max}$
5. Check the difference between the IQR calculated in step 3 using ESM  $TS_{m,s}^{min/max}$  values and that calculated using observational  $TS_{m,s}^{night/day}$  values. A positive difference indicates more spread within the biases for  $TS_{m,s}^{min/max}$  derived  $T_{m,s}^{2m}$  values, in which case the biases are not acceptable considering those arising from natural variability within the observational data.

265 A separate multivariate Gaussian process is constructed for the observational  $TS_{m,s}^{night/day}$  and ESM  $TS_{m,s}^{min/max}$  values in Step 1. In order to construct the Gaussian process we first test the observational  $TS_{m,s}^{night/day}$  and ESM  $TS_{m,s}^{min/max}$  values for normality using a Shapiro-Wilk test (see Figures C1-C4 in Appendix C). Observational  $TS_{m,s}^{night/day}$  values are normally distributed over all grid points, while ESM  $TS_{m,s}^{min/max}$  values show some grid points (at most 17% of grid points) where the null hypothesis of being normally distributed is rejected. Given that this is less than half of the grid points we proceed with  
 270 applying the multivariate Gaussian process.

### 3.4 Emulating 2-m air temperature responses to tree cover changes within the SSP scenarios

By predicting the expected surface temperature responses using the calibrated  $\Gamma_m$  (described in Section 3.2.1), and subsequently diagnosing the corresponding 2-m air temperature response using Equation 3; we can emulate the expected 2-m air temperature response to tree cover changes over the whole land area for any land cover change scenario. In this study, we do so

---

<sup>1</sup>removed: 95%

275 for 2 Shared Socioeconomic Pathways – SSP2 1-2.6 and SSP3-7.0 – for which the underlying narratives and resulting changes  
in tree cover over the 21st century are presented in Section 2.3. We only present the results for changes in tree cover between  
2015 and the end of the century (mean changes between 2015 and 2100).

In arriving at the final 2-m air temperature response emulations, we are mindful of the limited training data available for  
constructing  $\Gamma_m$ . To account for this, we assess the underlying signal-to-noise ratio in the emulations, by considering "noise" as  
280 the parametric uncertainties within  $\Gamma_m$  conditional on the training sample population. The noise in emulations arising from the  
parametric uncertainties within  $\Gamma_m$ , is evaluated using a parametric bootstrap procedure (Hastie and Tibshirani, 1986; Wood,  
2017). In the following sections, we outline the parametric bootstrap procedure used, followed by how its results allow for  
evaluation of the signal-to-noise ratio in the final 2-m air temperature response emulations.

### 3.4.1 Estimating parametric uncertainty in the predicted temperature responses

285 We quantify the impact of parametric uncertainties within  $\Gamma_m$  on the  $\Delta T S_{m,s}$  predictions following a parametric bootstrap  
method as outlined in Figure 2 (Wood, 2017; Efron and Tibshirani, 1993). Parametric bootstrapping constitutes of first ap-  
proximating the joint distribution of the coefficients ( $\beta$ ) and  $\lambda$  parameter used within  $\Gamma_m$ , conditional on the training data  
available i.e.  $f(\beta, \lambda | \mathbf{X})$  (Step 1, Figure 2), from which  $\beta$  values are then sampled to estimate surface temperature responses  
(Step 2, Figure 2). To avoid high computational costs, the joint distribution is approximated by first bootstrap sampling the  
290 distribution of  $\lambda$  conditional on the training material, i.e.  $f_\lambda(\lambda)$  (Steps 1a-1b, Figure 2), from which the distribution of  $\beta$   
conditional on both  $\lambda$  and the training material is constructed over the whole  $f_\lambda(\lambda)$  space (Step 1c, Figure 2), such that  
 $f(\beta, \lambda | \mathbf{X}) \approx f(\beta | \lambda, \mathbf{X}) \cdot f_\lambda(\lambda)$ . Surface temperature response values are then sampled by drawing  $\beta$  distributions from ran-  
dom parts of the  $f_\lambda(\lambda)$  space (Step 2a, Figure 2) and sampling coefficient values from them (Step 2b, Figure 2), which are then  
used to estimate  $\Delta T S_{m,s}$  values (Step 2c, Figure 2).

### 295 3.4.2 Evaluating signal-to-noise in the predicted temperature responses

In representing temperature responses under new tree cover change scenarios, we consider the signal-to-noise ratio in the  
final  $\Delta T_{m,s}^{2m}$  emulations. "Noise" constitutes the underlying parametric uncertainty within  $\Gamma_m$  arising from the training sample  
population. We start by sampling  $\Delta T S_{m,s}^{min/max}$  values from  $\Gamma_m^{min/max}$  globally for each relevant pixel using the parametric  
bootstrap procedure outlined in Section 3.4.1, and then diagnose  $\Delta T_{m,s}^{2m}$  for each sample. The  $\beta$  and  $\lambda$  parameter uncertainty  
300 spaces are constructed using 10 bootstraps from which 200 samples are then drawn. We take the mean across all samples as  
the expected  $\Delta T_{m,s}^{2m}$  value and the standard deviation across all samples as the underlying parametric uncertainty within the  
GAM. The signal-to-noise ratio is then obtained as the ratio between the mean and standard deviation values. We consider  
emulations with a signal-to-noise ratio lower than 0.5 as insignificant, as the underlying parametric uncertainty is double  
the actual magnitude of expected response. Given the computational expenses of running ESMs, such gives  $\Gamma_m$  the benefit  
305 of mainly requiring extreme tree cover change scenarios as training material, from which it can further explore all possible

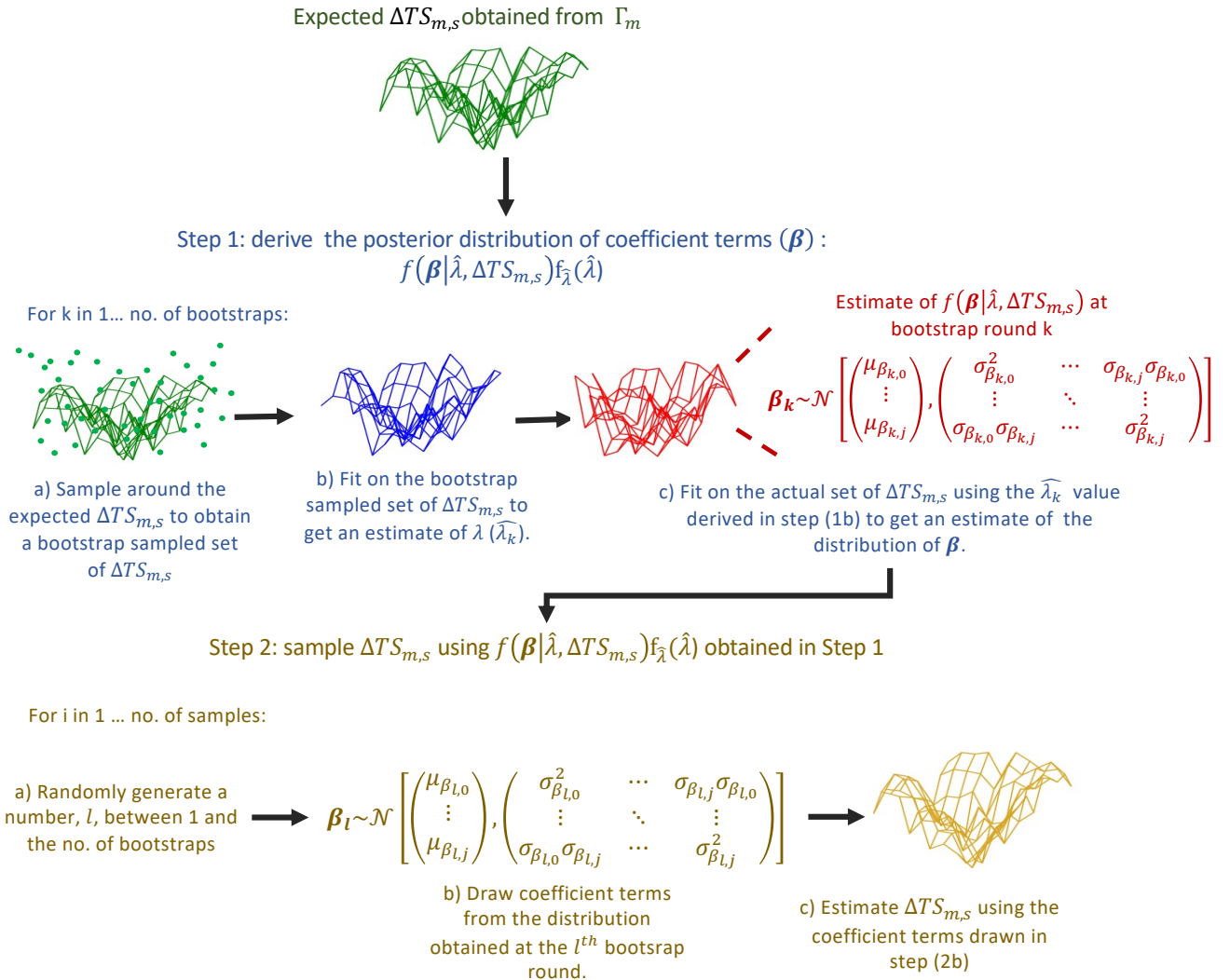


**Figure 2.** Sampling routine of the Generalized Additive Model. First, an approximation of the coefficients' ( $\beta$ ) and  $\lambda$  parameter's joint distribution given the available training data is constructed (Step 1), from which coefficient terms are sampled to calculate  $\Delta TS_{m,s}^{mean}$  values with (Step 2). Steps 1a-1b construct the sampling distribution of the  $\lambda$  parameter ( $f_{\lambda}(\lambda)$ ) given the known variability in the training data, and Step 1c then constructs the distribution of  $\beta$  conditional on the training data and  $\lambda$  parameter at each point of the  $f_{\lambda}(\lambda)$  space. As such, the  $\Delta TS_{m,s}^{mean}$  values calculated in Step 2 account for the uncertainty in the shape of  $\Delta TS_{m,s}^{mean}$  responses, as modulated by  $\beta$  and  $\lambda$  values.

outcomes of in-between scenarios itself. It should be noted however that this does not remove the benefit of having more training material on top of the extreme scenarios, but simply minimises the training data requirements of  $\Gamma_m$ .

## 4 Results

### 4.1 Blocked cross validation results

310 In this section we show the calibration and evaluation results of  $\Gamma_m^{mean}$ , obtained by performing different sets of blocked cross-validation as [..<sup>2</sup>]described in Sections 3.2.2 and 3.2.3. The calibration and evaluation results for example months of January and July, which are representative of the hottest and coldest months for the Northern Hemisphere and vice versa for the Southern Hemisphere, are shown. First, we show results from the blocked cross validation used to calibrate  $\Gamma_m$  for its optimal  $\lambda$  parameter and number of basis functions (Section 4.1.1). Second, we show the results of the blocked cross validations employed  
315 to evaluate the calibrated  $\Gamma_m$ 's performance into "no-analogue" conditions. "No-analogue" conditions of background climate (Section 4.1.2) and those of tree cover change amounts (Section 4.1.3) are considered specifically with a separate blocked cross validation performed for each. The following subsections show the blocked cross validation results for  $\Gamma_m^{mean}$  only as this gives a representative idea of the validity of this study's framework. Blocked cross validation results for  $\Gamma_m^{min/max}$  are provided in the Appendix B.

#### 320 4.1.1 Results of model calibration

Figure 3 provides the best performing  $\lambda$  parameter values and number of basis functions (nbf) configuration for  $\Gamma_m^{mean}$ [..<sup>3</sup>]. Maps of RMSEs calculated between the mean surface temperature response  $\Delta T S_{m,s}^{mean}$  [..<sup>4</sup>]samples drawn by the fully calibrated  $\Gamma_m^{mean}$  (200 samples are drawn as described in Section 3.4.1), for the tree cover changes  $\Delta treeFrac_{2015}$  implemented in the ESM experiments used for training, and the values actually simulated by the ESMs are further provided.  
325 The percentage of grid points with RMSE values below 0.5 are indicated above each map. These results are shown for both the DEF and AFF scenarios (only DEF for observations).

The  $\Gamma_m^{mean}$  trained on observational data has a  $\lambda$  parameter value of 0.001 for both January and July, which is significantly lower than that of 1 otherwise chosen for all ESMs. This could be as the observationally trained  $\Gamma_m^{mean}$  only receives training data for the DEF scenario, which implements large magnitudes of tree cover change localised to specific regions (see Figure  
330 A1). Thus, lower  $\lambda$  parameter values are favoured to allow for complex representation with higher spatial variability. The observationally trained  $\Gamma_m^{mean}$  moreover shows poor performance with only 34% of grid points have RMSE values less than 0.5. This possibly arises from less training data available for the observationally calibrated  $\Gamma_m^{mean}$  (i.e., less grid points as well as only one tree cover change scenario), such that  $\Gamma_m^{mean}$  cannot gain as much information to predict with.

All ESMs show higher RMSEs, with a lower proportion of grid points having RMSE values <0.5, for the DEF scenario than  
335 the AFF scenario. This could be related to difficulty in representing the complex response types with high spatial variabilities within the DEF scenario. Such highlights a design consequence of  $\Gamma_m^{mean}$ , where  $te_m$  is fitted smoothly over  $lon$ ,  $lat$  and  $\Delta_{2015}treeFrac$ , thus falling short in representing high spatial variabilities as brought about by large magnitudes of localised

---

<sup>2</sup>removed: dexcribed

<sup>3</sup>removed: , alongside maps of the RMSEs between its predicted expected response of

<sup>4</sup>removed: to

tree cover change. While CESM2 and EC-EARTH show varying number of grid points with RMSE values below 0.5 between January and July for the AFF and DEF scenarios, MPI-ESM shows similar performance across both months for the Aff and DEF scenarios. Additionally, MPI-ESM's  $\Gamma_m^{mean}$  favours the simplest representation across all ESMs with the lowest number of basis functions chosen for both January and July. Such indicates a smoother response type outputted by MPI-ESM, with deforestation in the tropics not necessarily leading to significant temperature jumps within space.

Overall,  $\Gamma_m^{mean}$  mostly displays RMSEs less than or equal to 0.5 for all ESMs. Higher RMSEs ( $>0.5$ ) are usually localised to regions of extreme magnitudes of deforestation for CESM2 and EC-EARTH. In the case of MPI-ESM, higher RMSEs are localised to different regions depending on the month. For example in both AFF and DEF scenario, MPI-ESM shows higher RMSEs over South South America and Australia in January and over the South North America and the Mediterranean region for July. In such,  $\Gamma_m^{mean}$  proves itself as a reasonably flexible framework to represent expected temperature responses to more realistic magnitudes of tree cover change. As noted in the observationally calibrated  $\Gamma_m^{mean}$ , a substantial hindrance to  $\Gamma_m^{mean}$ 's performance is the availability of training data, where it is recommended to have both directions (i.e., positive and negative) of tree cover changes available for training.

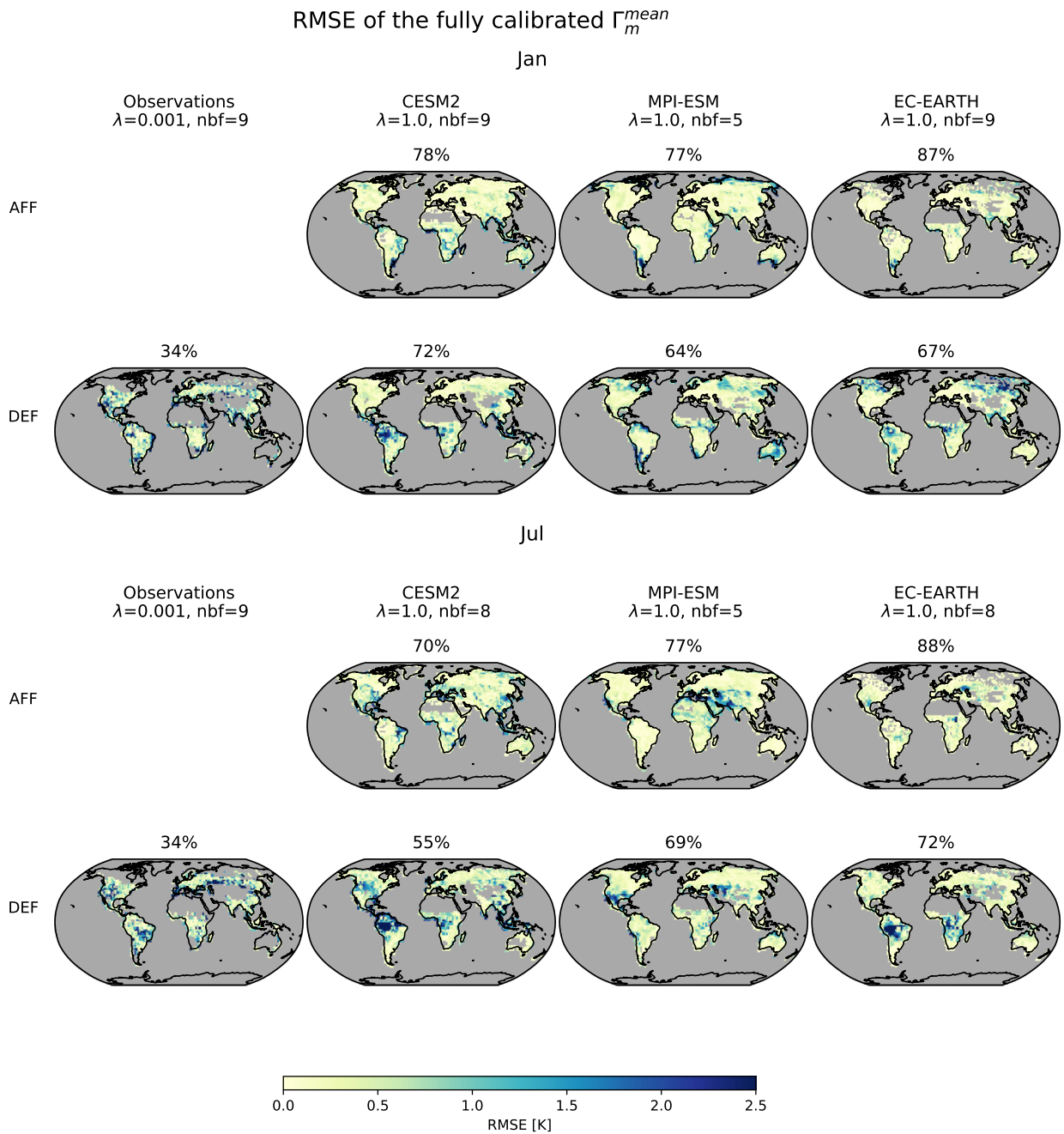


**Figure 3.** Performance of the fully calibrated  $\Gamma_m^{mean}$  trained on each full set of observational/ESM data for example months of January (upper panel) and July (lower panel) shown as RMSE maps (rows) for afforestation, AFF (first row), and deforestation, DEF (second row), scenarios. Columns headers indicate the training dataset used and the respective  $\lambda$  parameter and number of basis functions (nbf) chosen during blocked cross validation. Percentages above each map indicate the proportion of land area with RMSE values less than 0.5.



#### 4.1.2 Evaluation of $\Gamma_m^{mean}$ under "no-analogue" background climates

Figure 4 shows RMSEs obtained for  $\Gamma_m^{mean}$ 's <sup>5</sup> sampled predictions (200 samples are drawn as according to Section 3.4.1) into "no-analogue" background climates aggregated to latitudinal bands for example months of January and July. Latitudinal bands were chosen as representative of the different  $\Delta TS_{m,s}$  response types to tree cover changes – as seen in  
355 De Hertog et al. (2022) – namely: northern-hemispheric, temperate (40°N to 65°N); subtropical, temperate (10°N to 40°N); tropical (-15°N to 10°N); and southern-hemispheric (-45°N to -15°N). Southern-hemispheric results are not differentiated into subtropical and temperate as the sample size of predictions would become too small otherwise. RMSEs are differentiated into those obtained under the AFF scenario and the DEF scenario, except for observations where RMSEs are only available for the DEF scenario.

360 For observations and ESMs, the spread in RMSEs displays a month dependency across all latitudinal bands, evidencing the seasonality in  $\Delta TS_{m,s}^{mean}$  responses to tree cover change as well as the need for prior background climate information being more important for certain months than others. Despite the spread in RMSEs being large, median values are mostly below 0.5 for ESMs and below 1.5 for Observations, which is in line with those seen in Figure 3, indicating overall good prediction skill for  $\Gamma_m^{mean}$  into unseen background climate conditions. Observation RMSEs for DEF in -45 °N to -15 °N however show  
365 significantly higher median values than those in Figure 3, although this is more likely due to data sparsity within the training data for this region, leading to little information learned by the observationally calibrated  $\Gamma_m^{mean}$  for this region.

Across ESMs, DEF in the tropics (-15 °N to 10 °N) shows the largest spreads in RMSEs with slightly higher median values than those of Figure 3. Given that  $\Gamma_m^{mean}$  may struggle within these areas due to the localised, large magnitudes of deforestation (as seen for CESM2 and EC-EARTH in Figure 3), exploration of its performance into "no-analogue" tree cover changes is first  
370 required before concluding lower prediction skill for unseen background climate conditions within these areas.

#### 4.1.3 Evaluation of $\Gamma_m^{mean}$ under "no-analogue" tree cover change amounts

Figure 5 shows the median RMSEs (with error bars indicating 50% confidence intervals) obtained for  $\Gamma_m^{mean}$ 's sampled predictions into "no-analogue" tree cover changes aggregated to latitudinal bands for example months of January and July. For observations and ESMs, magnitudes and patterns of RMSEs are similar between January and July across all latitudinal  
375 bands, contrary to what has been found for the predictive ability in "no-analogue" background climate conditions 4.1.2. This is expected as, the way that local temperature response to tree cover changes depends on the season varies across background climates (and mainly across the latitudes, see for example Li et al. (2015)), and is thus intuitively more important for representing seasonality in  $\Delta TS_{m,s}^{mean}$  values.

Median RMSEs for  $\Delta_{2015} treeFrac \leq -0.5$  in the tropics are higher than those seen for DEF in Figure 4, indicating that the  
380 prediction skill for  $\Gamma_m^{mean}$  in the tropics is more dependent on the availability of training information for similar tree cover changes than for similar background climate. MPI-ESM is an exception to this, displaying much larger RMSEs for DEF in Figure 4. Such could result from MPI-ESM outputting a weaker response to tree cover change in the tropics as previously

---

<sup>5</sup>removed: predictions

suggested in Section 4.1.1, making availability of prior background climate information the main factor influencing  $\Gamma_m^{mean}$ 's prediction skill.

385 Observations, CESM2 and EC-EARTH show an increase in RMSEs across all latitudinal bands as  $\Delta_{2015}treeFrac$  values move towards the more extreme ends (-1 for observations and +/-1 for CESM2 and EC-EARTH), sometimes even reaching RMSEs higher than those seen in Figure 3. This indicates lower prediction skill for  $\Gamma_m^{mean}$  into unseen, extreme tree cover change conditions for observations, CESM2 and EC-EARTH. Nevertheless, the resolved skill seen in Figure 3 verifies the need to have a training dataset representative of the extreme ends of tree cover change, as  $TS_{m,s}^{mean}$  responses may systematically  
390 become more non-linear with increasing magnitudes of tree cover change.

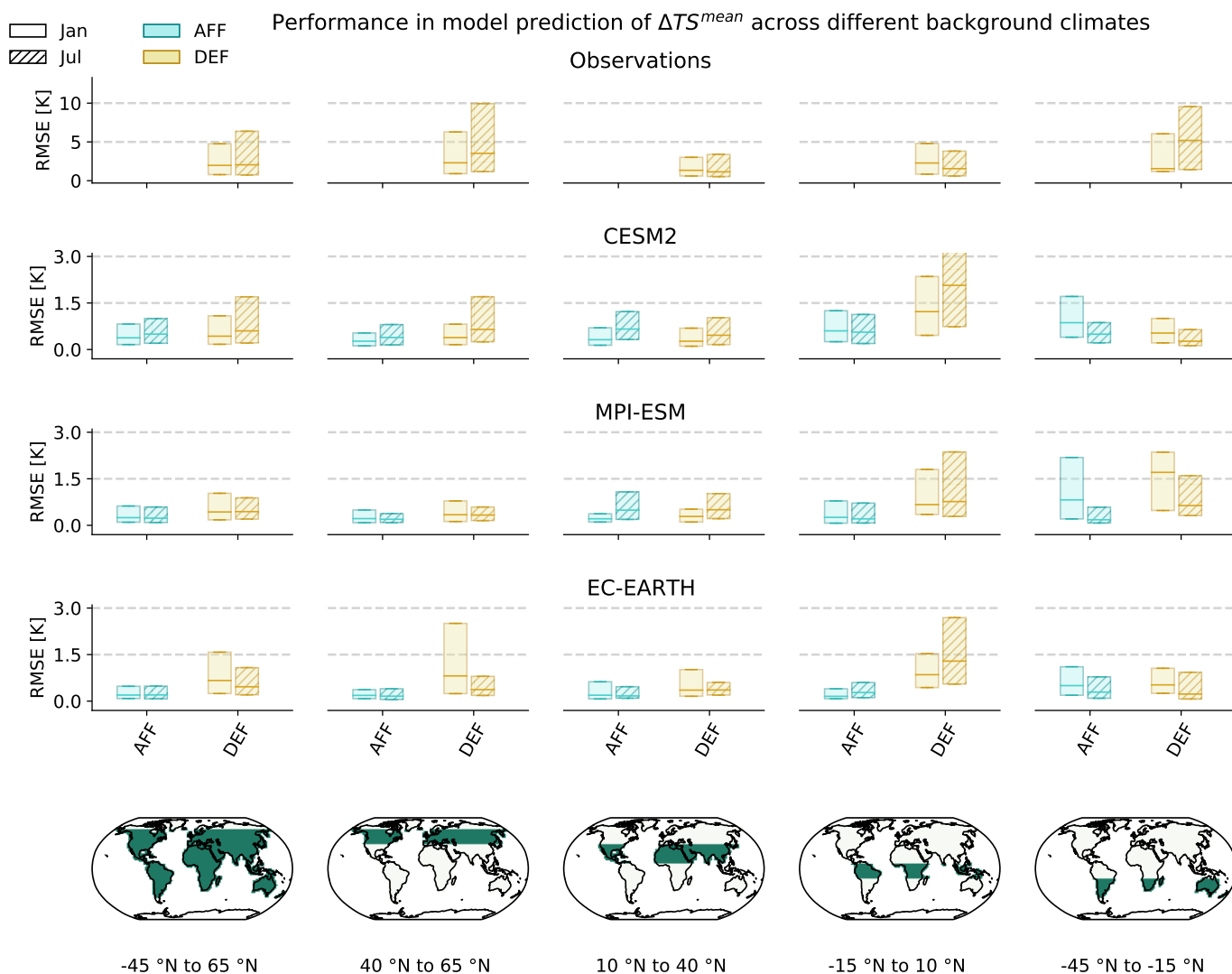


**Figure 4.** Evaluation of  $\Gamma_m^{mean}$ 's predictive ability under 'non-analogue' background climate conditions. Test set RMSEs obtained during blocked cross validation with blocks clustered according to background climate and continuous geographical region (as shown in Figure A1) are considered. RMSEs are shown for the months of January (unhatched) and July (hatched) and are aggregated to latitudinal band (columns) and direction of tree cover change, yellow indicating a negative change (DEF) and blue indicating a positive change (AFF). The box-plots indicate the median RMSEs as well as the associated interquartile ranges. Note that the scale used for Observations (upper row) is different.

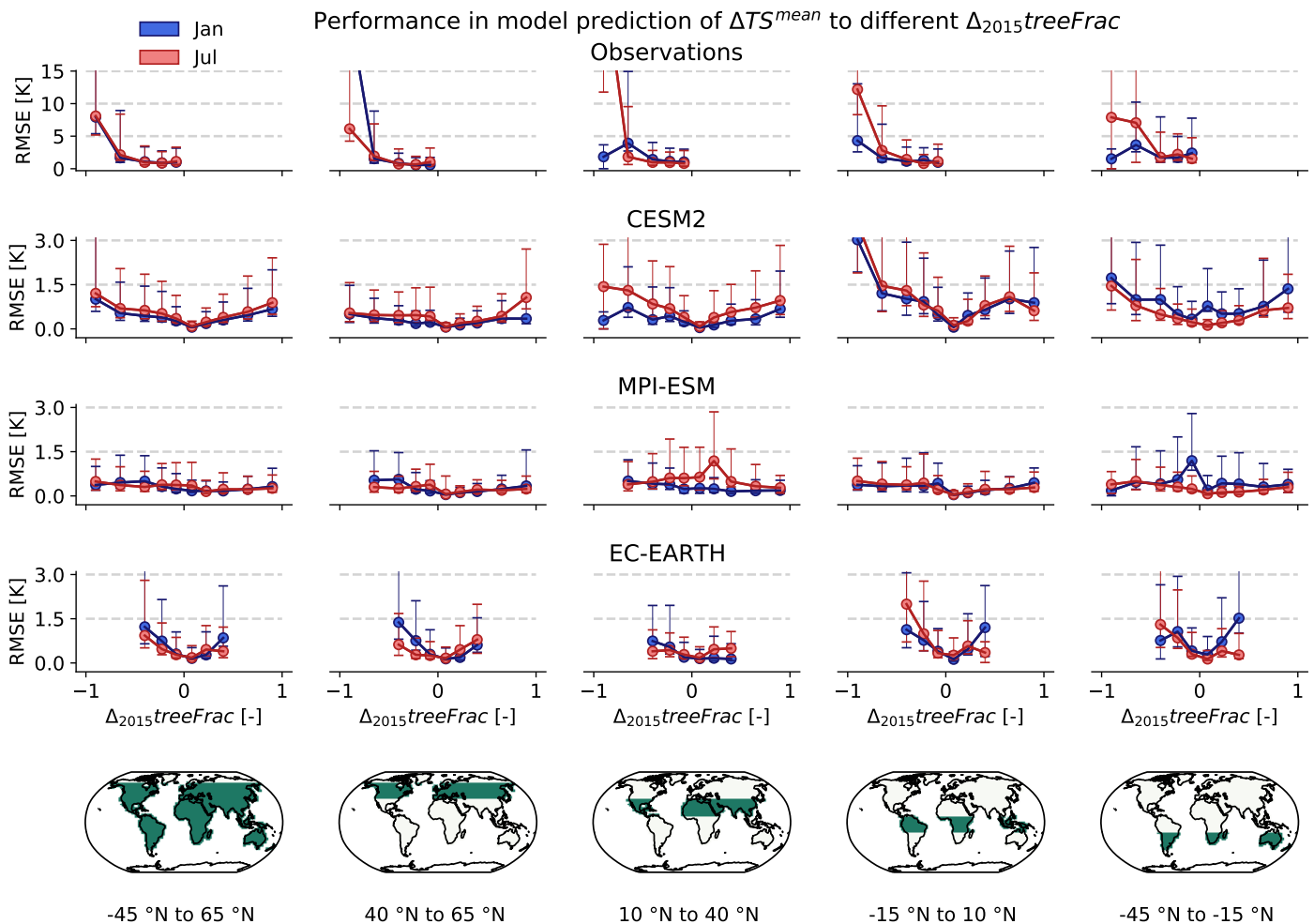


**Figure 5.** Evaluation of  $\Gamma_m^{mean}$ 's ability to predict across  $\Delta_{2015}treeFrac$ . Test set RMSEs were obtained during blocked cross validation using blocks identified by gathering grid cells that underwent similar  $\Delta_{2015}treeFrac$  (grouped according to sign of change and absolute value as binned into  $[0.01,0.15)$ ,  $[0.15-0.3)$ ,  $[0.3-0.5)$ ,  $[0.5-0.8)$  and  $[0.8-1.0]$  within continuous geographical regions. RMSEs are shown for January (blue) and July (red), are aggregated to latitudinal bands (results for each band are shown in a different column) and plotted against the centre of each  $\Delta_{2015}treeFrac$  bin. The dots indicate the median RMSEs, while the error bars indicate the associated interquartile range. Note that the scale used for Observations (upper row) is different.

## 4.2 Illustration of $\Gamma_m^{mean}$ outputs

In this section, we showcase the results of  $\Gamma_m^{mean}$  when predicting  $\Delta T_{m,s}^{mean}$  for any amount of tree cover change compared to 2015 levels and across the world. A select tree cover change value is applied to all grid points, and  $\Gamma_m^{mean}$  then used to predict the temperature responses for that tree cover change. Figure 6 illustrates the mean  $\Delta T_{m,s}^{mean}$  predictions as well as their 95% interval calculated across all grid points within a given latitudinal band. We choose the same latitudinal bands used in Figures 4 and 5  $T_{m,s}^{mean}$

As a preliminary check, the predictions can be roughly compared to the ESM outputs for the idealised AFF and DEF simulations as analysed by De Hertog et al. (2022). Only a rough comparison is possible however, as we generate predictions for tree cover change maps of constant values across grid points, whereas the tree cover change maps applied within the AFF/DEF scenarios vary in values across grid points since they represent full expansion of forest/cropland relative to the 2015 period. To this extent,  $\Delta T_{m,s}^{mean}$  predictions shown in Figure 6 correspond well in terms of direction and magnitude to the results shown in Duveiller et al. (2018) (for observations) or De Hertog et al. (2022) (for ESMs, compare with their Figures 2, 3, 5 and 6). For example, over the northern hemispheric temperate region (40°N to 65°N) in January,  $\Gamma_m^{mean}$  indicates a cooling (warming) following deforestation (afforestation) when trained on all ESMs and observations, while the temperature response in July is less clear but still rather indicates a warming from deforestation over these regions. [.6] Moreover,  $\Gamma_m^{mean}$  is notably able to capture the inter-ESM spread in  $\Delta T_{m,s}^{mean}$  values. For example, in the latitudinal band 40°N to 65°N, EC-EARTH-based predictions show a cooling trend after +25% tree cover change, in contrast to the warming trend seen in other ESMs. Such a difference was also noted in De Hertog et al. (2022) and attributed to lower amounts of boreal afforestation implemented.

Over all latitudinal bands and months shown, the largest 95% intervals occur towards the extreme ends of tree cover change for both observations and ESM-based predictions. This is especially the case for deforestation, where the 95% intervals are in general larger than those of afforestation. Higher 95% intervals at extreme ends of tree cover change results from less grid points which undergo more extreme tree cover changes, ergo less training material. This highlights once more the higher uncertainty in the predictions by  $\Gamma_m^{mean}$  for extreme amounts of tree cover changes (in both directions).

Mean observation-based predictions remain close to 0 across all latitudinal bands for both January and July, owing to the high data sparsity which makes it difficult to extract significant  $T_{m,s}^{mean}$  responses during training. Nonetheless, observation-based 95% intervals are in general agreement with those of ESMs across all latitudinal bands and months shown.

## 4.3 Surface to 2-m air temperature diagnosis

In this section, we apply the modified Hooker et al. (2018) model (Equation 3) to the outputs of  $\Gamma_m^{min}$  and  $\Gamma_m^{max}$  so as to derive the expected  $T_{m,s}^{2m}$  responses to tree cover change. Results are only shown for CESM2, as tree cover changes implemented in the experiments run by this ESM cover the whole range of possible  $\Delta_{2015}treeFrac$  (unlike observations and EC-EARTH) and provide local  $T_{m,s}^{min/max}$  values (not available from MPI-ESM otherwise). We first ascertain that applying Equation 3 in

---

<sup>6</sup>removed: Similarly,  $\Gamma_m^{mean}$  indicates that deforestation entails a local warming which is in addition lower in MPI-ESM.

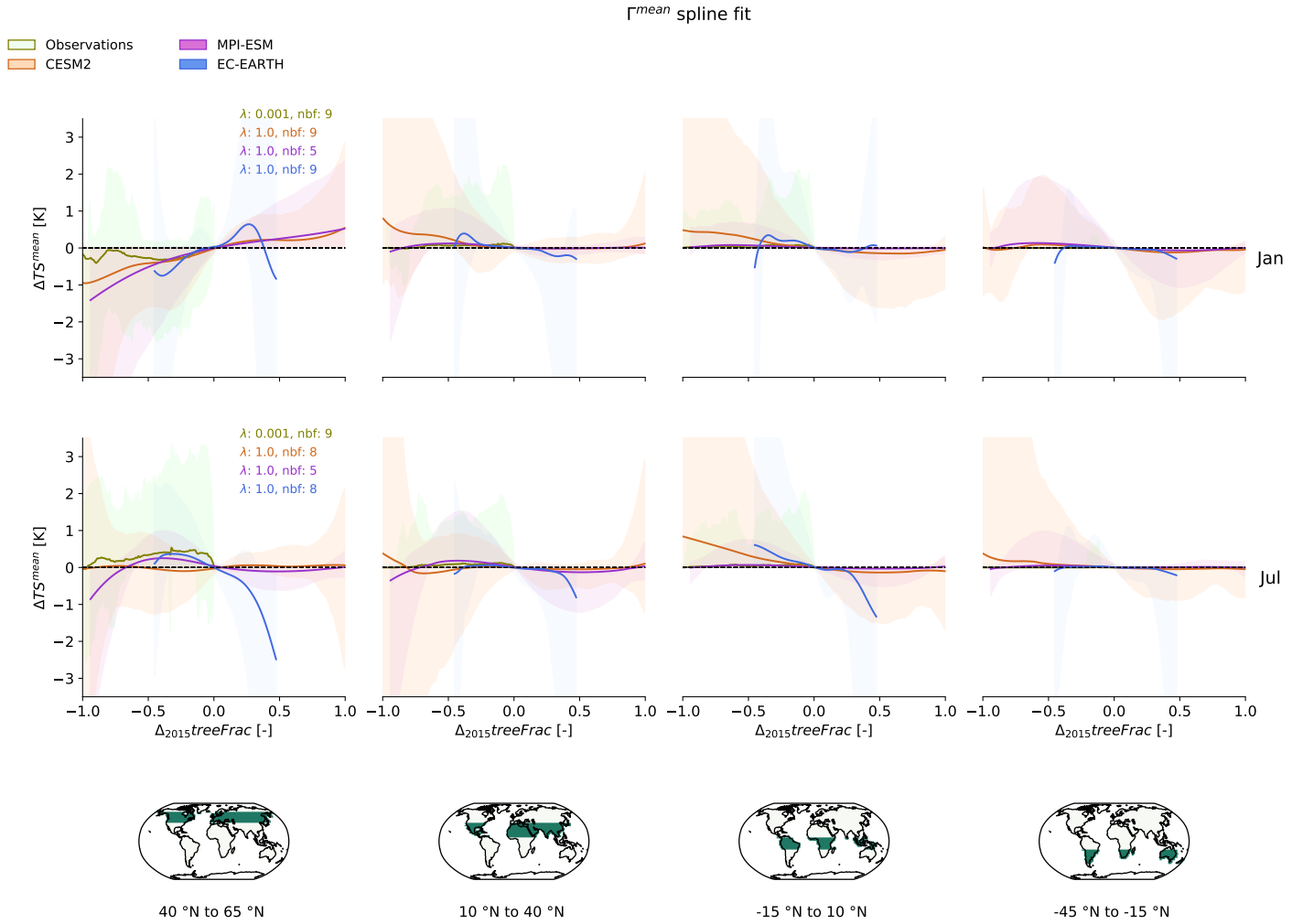


**Figure 6.**  $\Gamma_m^{mean}$ 's depiction of  $\Delta TS_{m,s}^{mean}$  shown for observations and ESMs (colours) at months of January (first row) and July (second row) across the whole range of  $\Delta_{2015}treeFrac$  and aggregated to latitudinal bands (columns).  $\lambda$  parameters and number of basis functions (nbf) chosen through blocked cross validation are given in the first column of their respective month and colour coded according to their respective training data (observations or ESMs). Solid lines represent the mean  $\Delta TS_{m,s}^{mean}$  predictions and the surrounding band represents the 95% interval calculated over  $\Delta TS_{m,s}^{mean}$  predictions for all grid-points within the respective latitudinal band.

the ESM space does not introduce additional biases to  $T_{m,s}^{2m}$  predictions on top of those arising from the natural variability in observed values, after which we proceed with predicting  $T_{m,s}^{2m}$  responses based off  $\Gamma_m^{min/max}$  outputs.

### 425 4.3.1 Tests on the modified Hooker et al. (2018) model applied to the ESM space

Figure 7 compares the spread of biases in  $T_{m,s}^{2m}$  calculated using ESM values to that obtained when using observational values. Positive values indicate more spread within the biases of ESM derived  $T_{m,s}^{2m}$  values, suggesting that biases outside the range of those arising from natural variability may occur when calculating  $\Delta T_{m,s}^{2m}$ .

430 Across most months, less than 40% of grid points have positive values, and these mostly occur in the Northern Hemisphere for the months between and including January and June. Such may result from the change in length of day during these months such that  $TS_{m,s}^{min/max}$  values do not necessarily correspond to the  $TS_{m,s}^{night/day}$  values. To be specific, the time of overpass for measuring  $TS_{m,s}^{night}$  and  $TS_{m,s}^{day}$  are fixed at 0100 and 1300 respectively, however given the longer nights in Northern-hemispheric winters,  $TS_{m,s}^{min}$  are likely to occur later and  $TS_{m,s}^{max}$  earlier than these times.

### 4.3.2 2-m air temperature diagnoses

435 Since less than half of grid points have positive values and such values are isolated to certain months and geographical areas, we proceed with diagnosing  $\Delta T_{m,s}^{2m}$  from  $\Delta TS_{m,s}^{min/max}$  values outputted by  $\Gamma_m^{min/max}$ . The calibration and evaluation results for  $\Gamma_m^{min/max}$  are available in Appendix B and show similar results as those seen in Section 4.1, namely minimal additional RMSEs when predicting into "no-analogue" conditions sampled out of the training dataset as compared to when predicting after having seen the full training dataset (i.e. comparing RMSE values from Figures B3 and B4 to those of Figure B2). It should be noted that  $\Delta TS_{m,s}^{max}$  predictions show high RMSEs, especially for the DEF scenario where less than half of the grid points have RMSEs lower than 0.5. In relation to the absolute  $\Delta TS_{m,s}^{max}$  values (see Figure B1) however, these RMSEs are of similar relative magnitude as those of  $\Delta TS_{m,s}^{min}$  and  $\Delta TS_{m,s}^{mean}$ . Moreover, RMSEs of  $\Gamma_m^{max}$  are of similar magnitude when predicting into "no-analogue" conditions as when predicting after having seen the whole training data set.

445 Figure 8 shows the  $\Delta T_{m,s}^{2m}$  values obtained at different tree cover change values, alongside the  $\Gamma_m^{min}$  and  $\Gamma_m^{max}$  predictions for example months of January and July. Patterns of  $\Gamma_m^{min}$  and  $\Gamma_m^{max}$  predictions correspond well to one another and generally well to  $\Delta TS_{m,s}^{min/max}$  values as derived in another study using the same ESM (Meier et al., 2018). An exception here are Northern Hemispheric, July  $\Delta TS_{m,s}^{max}$  values for which a cooling was observed in Meier et al. (2018) in contrast to the warming seen in the training material used within this study (see Appendix B, Figure B1). Such discrepancy could arise from too large albedo responses shown by CESM2 and highlights the caveats of diagnosing  $\Delta T_{m,s}^{2m}$  from  $\Delta TS_{m,s}^{min/max}$ , where physical inconsistencies in the surface temperature responses as represented within ESMs can be transferred to  $T_{m,s}^{2m}$  during diagnosis. 450 Nevertheless, the task of  $\Gamma_m$  is to mimic ESM outputs irrespective of their 'realism' and to this end, the statistically derived relationships for  $\Delta TS_{m,s}^{min/max}$  to tree cover changes match those of the ESM outputs trained on.

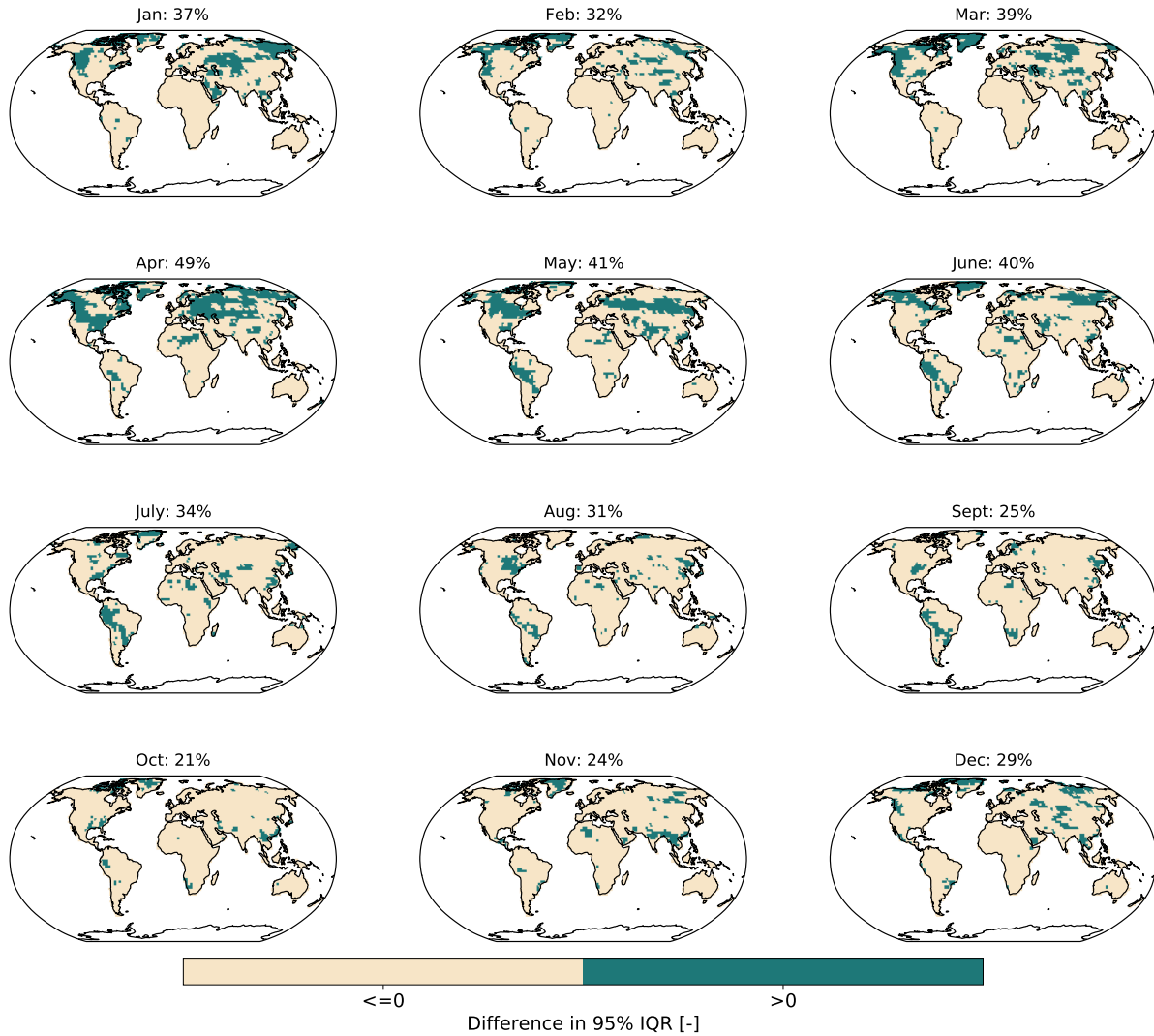


**Figure 7.** Differences between the spread of biases for ESM vs observationally derived  $T_{m,s}^{2m}$  values, obtained as described in Section 3.3. The inter-quartile range (IQR) is considered as a measure of spread and results are shown for CESM2 across all months. Percentage values indicate the proportion of land grid points where ESM-derived  $T_{m,s}^{2m}$  values have a larger spread in bias as compared to observationally derived  $T_{m,s}^{2m}$  values.



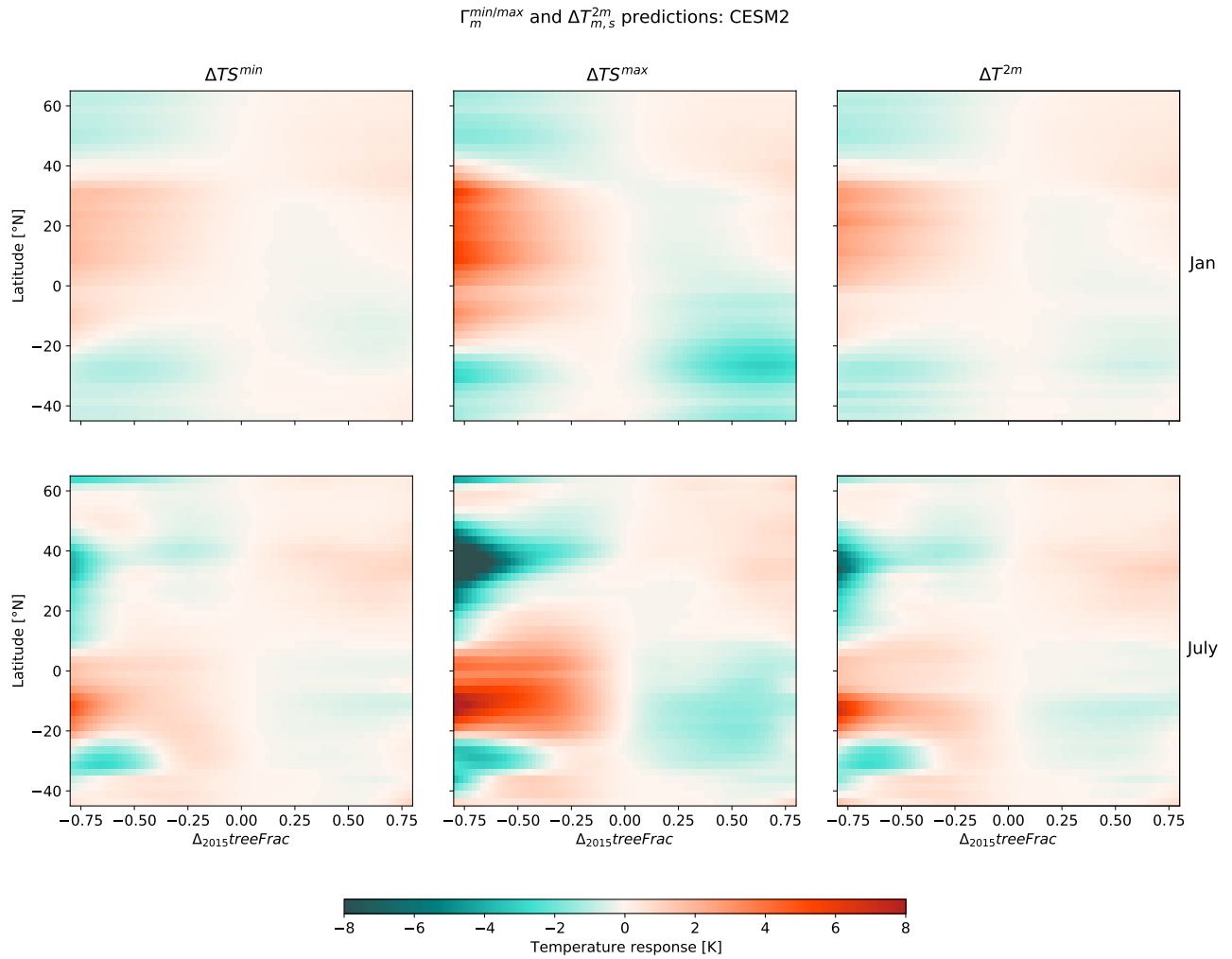


**Figure 8.** Latitudinally aggregated  $\Delta TS_{m,s}^{min/max}$  given by  $\Gamma_m^{min/max}$  (first two columns) shown for CESM2 at months of January (first row) and July (second row) across the full range of  $\Delta_{2015}treeFrac$ . The resulting  $\Delta T_{m,s}^{2m}$  values obtained using the modified Hooker et al. (2018) model are shown in the third column.

## 4.4 Exploration of tree cover change effects within SSP scenarios

In this section, we showcase the results of applying TIMBER v0.1 calibrated on simulations conducted with CESM2 to the scenarios of future tree cover changes in SSP1-2.6 and SSP3-7.0. We employ the sampling method as described in Section 3.4 such that parametric uncertainties within the GAM are also represented. This provides a first step towards statistically emulating  $T_{m,s}^{2m}$  responses to tree cover change, in a manner that not only provides the expected response, but also gives an idea of the signal-to-noise ratio within predictions.

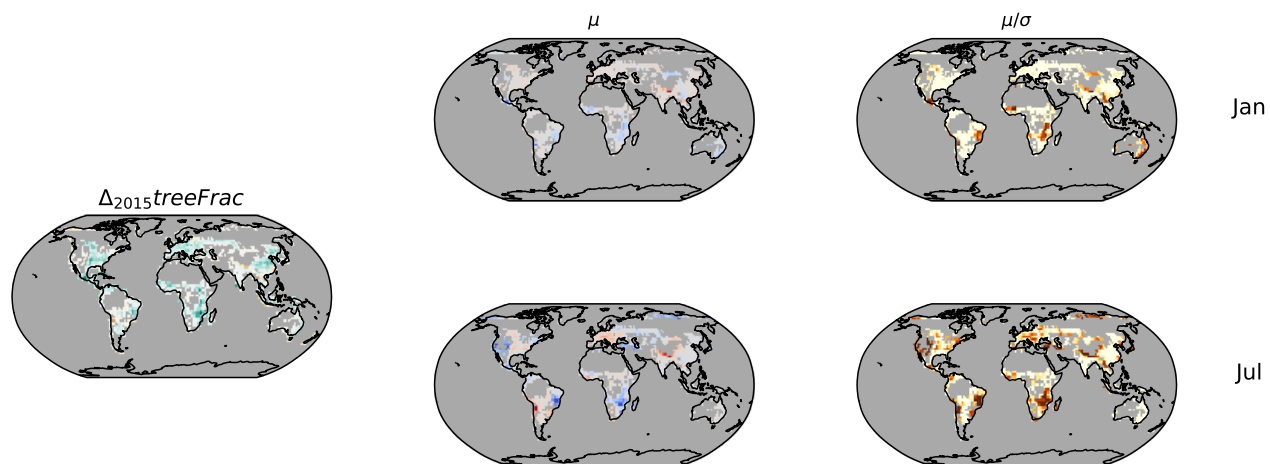
Figure 9 shows maps of end-of-century tree cover changes (shown in the first column) under SSP 1-2.6 and SSP 3-7.0 and their associated mean  $T_{m,s}^{2m}$  responses (second column), obtained by sampling  $\Delta T_{m,s}^{min/max}$  values from  $\Gamma_m^{min/max}$ , applying Equation 3 to get  $\Delta T_{m,s}^{2m}$  and taking its sample average. The signal-to-noise ratio is furthermore given by taking the ratio between the absolute mean  $\Delta T_{m,s}^{2m}$  value and its standard deviation calculated across sample results for  $\Delta T_{m,s}^{2m}$  (third column). We consider areas with a signal-to-noise ratio lower than 0.5 as having an insignificant temperature response, as their surrounding parametric uncertainty is double that of the magnitude of response.

SSP 1-2.6 shows substantial cooling from afforestation in Southern Africa and Brazil for both January and July. A substantial July warming due to deforestation can also be seen in the Tibetan plateau due to deforestation. SSP 3-7.0 shows a significant January and July warming due to deforestation in Central Africa, Tibetan plateau and South America. West-North America shows a significant cooling from deforestation especially in July, while parts of East Asia show significant cooling from afforestation for both January and July.

In general, areas with a tree cover change lower than 0.1 in magnitude tend to have a signal-to-noise ratio lower than 0.5 and thus an insignificant temperature response. Such systematically lower signal-to-noise ratios indicates that  $\Gamma_m$  is not only aware of the lack of information it has for smaller changes in tree cover, but can also infer that temperature responses to such tree cover changes are likely to be trivial.

Responses of  $T_m^{2m}$  to tree cover change under SSP scenarios: CESM2

SSP 1-2.6



SSP 3-7.0

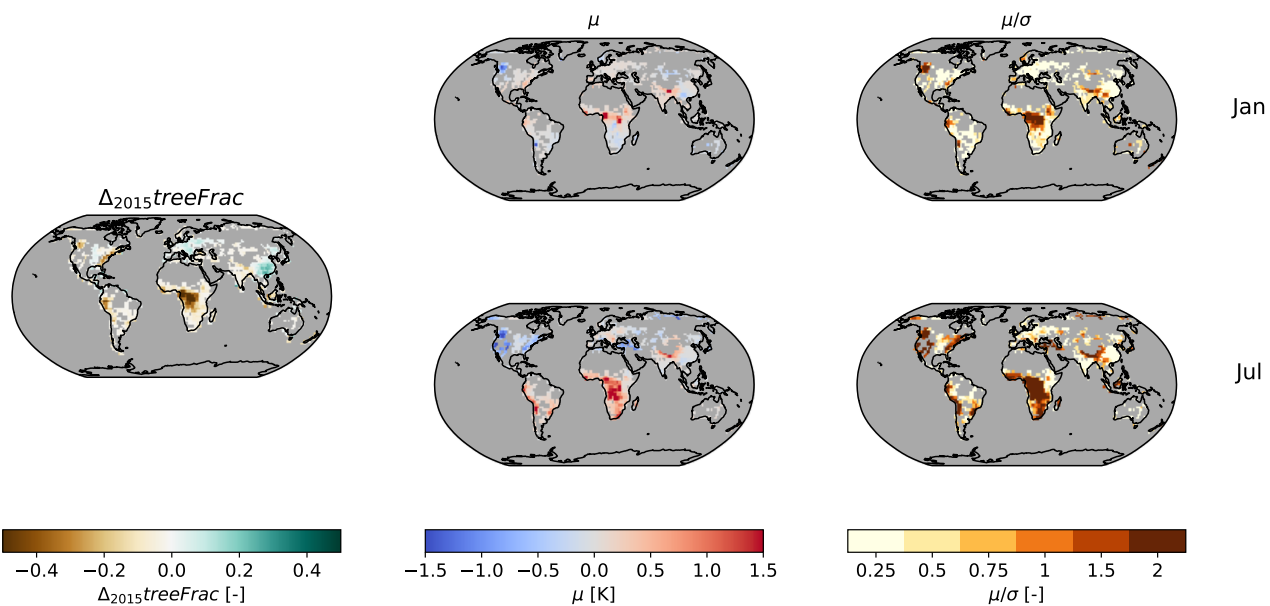


**Figure 9.**  $\Delta T_{m,s}^{2m}$  values resulting from end-of-century changes (i.e. 2100) relative to 2015 in tree cover for SSP 1-2.6 (upper panel) and SSP 3-7.0 (lower panel) scenarios at the months of January (top rows) and July (bottom rows). Mean  $\Delta T_{m,s}^{2m}$  values (second column) as well as their signal-to-noise ratios (third column) calculated over the sampling distributions are shown.  $\Delta_{2015}treeFrac$  maps are given in the first column, grid points with  $|\Delta_{2015}treeFrac| < 0.01$  are not considered.

## 5 Conclusion and Outlook

475 This study presents TIMBER v0.1, a conceptual framework for representing monthly temperature responses to changes in tree cover. TIMBER v0.1 starts by modelling minimum, mean and maximum surface temperature responses to tree cover change with a month-specific GAM which is trained over the whole globe. 2-m air temperature responses are then diagnosed from the modelled minimum and maximum surface temperatures using observational relationships derived by Hooker et al. (2018). Such an approach maintains the ESM-specific temperature response to tree cover change, whilst ensuring a constant diagnosis  
480 and observationally consistent definition of 2-m air temperature.

The GAM is evaluated for its ability to predict into unseen, i.e. "no-analogue", background climate as well as tree cover change conditions. This is done using a blocked cross validation procedure in order to account for the spatial structure of the data when splitting in subsamples used for training and testing. Overall, the GAM shows good skill in predicting into "no-analogue" conditions, with minimal additional RMSEs to those occurring when predicting after having seen the full training  
485 dataset and thus all available background climate and tree cover change information. Such provides confidence in the GAM's ability to derive meaningful relationships from the training data provided by the ESMs. Nevertheless, poorer representation for extreme, localised tree cover changes – such as deforestation in the tropics – was identified, most likely due to difficulty in adequately representing high spatial variability.

When predicting into new tree cover change scenarios, we are especially mindful of the training data only including grid  
490 points which experience extreme tree cover change in the training simulations. To this extent, surface temperature responses are sampled from the GAM, in a manner that explores all possible shapes of responses in between the two extreme ends of tree cover change as provided by the training data. 2-m air temperature responses are then diagnosed from the sampled surface temperature responses and relevant responses are identified as those having a high signal-to-noise ratio ( $>0.5$ ).

The final outputs of TIMBER v0.1 are demonstrated for SSP 1-2.6 and SSP 3-7.0. Generally, areas with less than  $\pm 10\%$  of  
495 tree cover change render a low signal-to-noise ratio, which is intuitive as responses to such low changes in tree cover are likely to be minimal. Employing TIMBER v0.1 thus provides avenue to explore impacts of tree cover change and their underlying uncertainty due to availability of training data and model calibration. It should be stressed that given the lack of comparable ESM simulations that employ the checkerboard approach to isolate local signals of land cover changes, TIMBER's outputs cannot be thoroughly validated, and must therefore be cautioned with the limitations of its current set up. Specifically, that they  
500 are produced with limited amounts of training data, as well as that the 2-m air temperature is diagnosed using observational relationships – as provided by Hooker et al. (2018) – directly applied to the ESM space. In the following subsections, we further highlight areas of potential improvement, elaborate upon the suitable modes of application for TIMBER v0.1 and detail possible further developments.

### 5.1 Areas of potential improvement

505 One area of potential improvement pertains to the model calibration procedure. When inspecting the calibrated  $\lambda$  parameter values and number of basis functions, the limits of values cross validated for (0.001 and 1 for the  $\lambda$  parameter and 5 and 9 for

the number of bases functions) seem to be favoured. Reasons behind this could be: (1) the blocked cross validation sometimes removes too large chunks of data, leading to an overestimation of RMSEs chosen, and/or (2) the range of  $\lambda$  parameter/number of basis functions values calibrated for is too narrow. The first reason could be tackled by further splitting the blocks such that each block has a predefined number of samples. Alternatively, the GAM could be fitted over specific climate regions, and blocked cross validation conducted with uniformly sized blocks composed along latitude and longitude dimensions; although here it is likely that the complete spectrum of tree cover change information will be lost for some regions. The second reason is easily solved by cross validating over a larger range of values.

Another area of improvement could be to derive ESM-specific coefficients for the Hooker et al. (2018) model. Such would entail fitting for the relationships between ESM minimum and maximum surface temperatures and the observational 2-m air temperatures as used by Hooker et al. (2018). Since the additional biases introduced by using the original Hooker et al. (2018) coefficients on the ESM surface temperatures were ascertained as minimal (Section 4.3.1), such an exercise would mostly target deriving the complete Hooker et al. (2018) model for each ESM. The resultant ESM-specific Hooker et al. (2018) models obtained would allow for more consistent 2-m air temperature diagnoses facilitating better comparison. Furthermore, considering that the difference between night and day surface temperatures (that are used as predictors in the original Hooker et al. (2018) model), and minimum and maximum surface temperatures may also be quite large (e.g. minimum winter temperatures in the Northern Hemisphere are likely to occur after the time of overpass when night time temperatures are measured), such would be an essential step to being able to accurately diagnose 2-m air temperatures.

## 5.2 Modes of application

TIMBER v0.1 provides a framework to explore local-level, temperature implications of tree cover changes in an agile manner under different tree cover change scenarios. TIMBER v0.1 can be used as both a standalone device as well as supplementary to other emulators. It should be noted that to provide complete representation of the biophysical effects of tree cover change, albedo and thermal fluxes would have to be considered as well. To this extent, the temperature responses provided by TIMBER arise from a combination of the effects of albedo and thermal flux responses to tree cover changes on the atmospheric energy balance. Here, we summarise some key take-aways pertaining to the use of TIMBER v0.1 for generating new tree cover change scenarios.

Upon inspection of the  $TS_{m,s}^{mean}$  response patterns across all tree cover changes (Figure 6), inter-ESM differences become quite apparent. Such differences are continuously studied and mainly arise from differences in model physical representation (Boisier et al., 2012; Lawrence et al., 2016; Lejeune et al., 2018; Davin et al., 2020; Boysen et al., 2020; De Hertog et al., 2022). Being able to train the GAM across all ESMs presents the opportunity to capture these uncertainties due to model physical representation, which may sometimes be higher than the parametric uncertainty within the GAM given the training data. When exploring new tree cover change scenarios, the need to have as many ESMs represented should therefore be emphasised. Moreover, the outputs of TIMBER v0.1 should always be interpreted as representative of the ESM-simulated world which does not necessarily translate to observed reality.

540 In applying TIMBER v0.1 to different tree cover change and climate scenarios, it should furthermore be acknowledged that the effects of initial starting conditions and those of background global warming levels have not been accounted for (e.g. see Winckler et al. (2017b) on the possible effects of initial starting condition on temperature responses to land cover changes). In order to represent such effects, TIMBER would require more training data. Nonetheless, the ESM experiments with which TIMBER is trained, use a 10-year spin up period and calculate the local temperature responses as averaged over the 150 year  
545 simulation period such that any background climate variations should also be averaged out. Hence, we expect the temperature response to tree cover change relationship derived by TIMBER to be reasonably robust across different initial starting and background climate conditions. Furthermore, if the Hooker et al. (2018) coefficients are recalibrated for the ESM space, impacts of changing climate on 2-m air temperatures could well be represented through the CSWR coefficients. Nonetheless, outputs of TIMBER v0.1 should more so be treated as hypothetical sensitivities and not definite responses.

550 Finally, as a conceptual framework, TIMBER v0.1 comes with its limitations that need to be accounted for and improved in future versions. A noteworthy limitation is the diagnosis of 2-m air temperature that relies on the modified Hooker et al. (2018) model. Such a set up was implemented so as to enable constant diagnosis and definition of 2-m air temperatures across ESMs and observations. However, since the original Hooker et al. (2018) model takes night and day surface temperatures as predictors, whereas the modified model used in this study takes minimum and maximum surface temper-  
555 atures, current 2-m air temperature predictions should be treated with caution. As seen in Figure 7, such differences are expected to introduce minimal biases since TIMBER looks at relative changes and not absolute values. However, for select months and regions (e.g. Winter in Europe and North America) there are still added biases as night and day surface temperatures do not necessarily correspond to minimum and maximum surface temperatures. An additional limitation to TIMBER is the lack of available ESM data to evaluate it against. Such a problem was circumvented in this study by  
560 synthesising the closest representation to "no-analogue" condition predictions for TIMBER. Nevertheless, when applying TIMBER to different scenarios, predictions should always be treated as approximations. To this extent, the signal-to-noise ratio calculations from TIMBER is an essential feature as it represents the model confidence in predictions based on the available training material.

### 5.3 Future Developments

565 It would be possible to extend TIMBER v0.1 to represent other impact-relevant climate variables. A variable to start with could be relative humidity, from which metrics such as Wet Bulb Globe Temperature (WBGT) and labour productivity could be derived. In doing so, variable cross-correlations between temperature and relative humidity should be conserved, such that compound events – which largely affect WBGTs – are sufficiently captured. To this extent, a Vectorised Generalised Additive Model (VGAM) (Yee and Stephenson, 2007) could be employed, which retains variable cross-correlations by constructing a  
570 multivariate conditional probability distribution e.g. by using a bi-normal distribution as opposed to the normal distribution used within this study. Another idea could be to couple TIMBER v0.1 to other emulators built to ingest temperature fields in order to generate additional climate variables. A suitable emulator for example could be PREMUS (Liu et al., 2022), which

is able to derive the principle modes of spatial variability from temperature fields, in order to generate monthly precipitation fields.

575 In its current set up, TIMBER does not differentiate between Plant Functional Types (PFTs). Temperature responses to tree cover changes however, may differ between different PFTs. For example, needleleaf trees in temperate regions are associated with a stronger winter warming as compared to broadleaf trees which otherwise lose their foliage during winter (Duveiller et al., 2018a). Representing the temperature responses to different PFTs instead of treating tree cover fraction as a single element would thus further enrich the outputs of TIMBER. A starting point to this could be differentiating between needle- and broad-  
580 leaf trees. Each of these tree types could be treated as separate tensor spline terms within the GAM, and the final temperature results would be obtained by adding both terms. When doing so, the potential model accuracy gained should be assessed in relation to the added model complexity (i.e. increase in the number of tensor spline terms). Given that needle- and broad- leaf trees are unevenly spread geographically (where broadleaf trees occur more in the tropics and needleleaf trees more in the temperate regions), it may also be worth training a separate GAM per geographical region, so as to get an even representation  
585 of needle- vs broad- leaf trees as well as as to prevent model overfitting.

Looking into other land management practices such as irrigation and wood harvest could also be of interest, particularly as their effects on surface temperatures are expected to be similar in magnitude as those due to land cover changes (Luyssaert et al., 2014). In doing so, customisation of TIMBER v0.1's framework to the LCLM practice of choice could be necessary. For example, when looking at irrigation, implementation of irrigation can be extremely localised and seasonal (Thiery et al.,  
590 2017, 2020) and it would be preferable to train the GAM as region-specific and across all months, instead of month-specific and across all grid-points. To this extent, the GAM has the advantage of not prescribing any functional form, giving it flexibility in deriving climate responses to different types of LCLM forcings regardless of the format of the training data.

In order to jointly explore future tree cover and GHG scenarios, coupling TIMBER v0.1 with other temperature emulators such as MESMER-M or -X (Beusch et al., 2020; Nath et al., 2022b; Quilcaille et al., 2022) also proves worthwhile. In doing  
595 so, care would have to be taken to not "double-count" the tree cover change signal as MESMER-M and -X are trained on SSP runs, which contain both GHG and tree cover change signals. Accordingly, it is advisable to first model the expected tree cover change signals within the SSP runs using TIMBER v0.1, following which MESMER-M or -X can be trained on the SSP runs with the modelled tree cover change signals removed.

*Code and data availability.* Data from the LAMACLIMA ESM experiments are archived on zenodo under the link, <https://doi.org/10.5281/zenodo.7261374>, (Nath et al., 2022a). Observational data used is available at Figshare, see reference Duveiller et al. (2018d). Code used for the emulator calibration, evaluation and sampling is archived on zenodo under the link, <https://doi.org/10.5281/zenodo.7261281> (Nath, 2022)  
600

*Author contributions.* QL, CFS and SIS identified the need for an emulator framework applied towards representing land cover forced climate responses. SN developed the emulator set up and calibration/evaluation procedure with help from QL, LG and JS. QL and GD  
605 furthermore assisted SN in integrating the observationally based, 2-m air temperature diagnosis scheme within the emulator. SDH, SQ, FH, FL, IM, JP and WT produced the ESM output. All authors contributed to interpreting results and streamlining the text.

*Competing interests.* The authors declare that they have no conflict of interest

*Acknowledgements.* We acknowledge that this study was conducted as part of the LAMACLIMA project, receiving funding from the German Federal Ministry of Education and Research (BMBF) and the German Aerospace Center (DLR) as part of AXIS, an ERANET initiated by  
610 JPI Climate (grant no. 01LS1905A), with co-funding from the European Union (grant no. 776608). SIS acknowledges partial support from the European Research Council (ERC) through the Proof-of-Concept Project MESMER-X (Project number: 964013). We furthermore thank members of the Work Package 1 of the LAMACLIMA project for running and providing the ESM training data. Steven De Hertog, Wim Thiery and Felix Havermann should particularly be acknowledged for their help in interpreting the LAMACLIMA outputs. We furthermore thank Edouard Davin for providing guidance in designing the emulator.



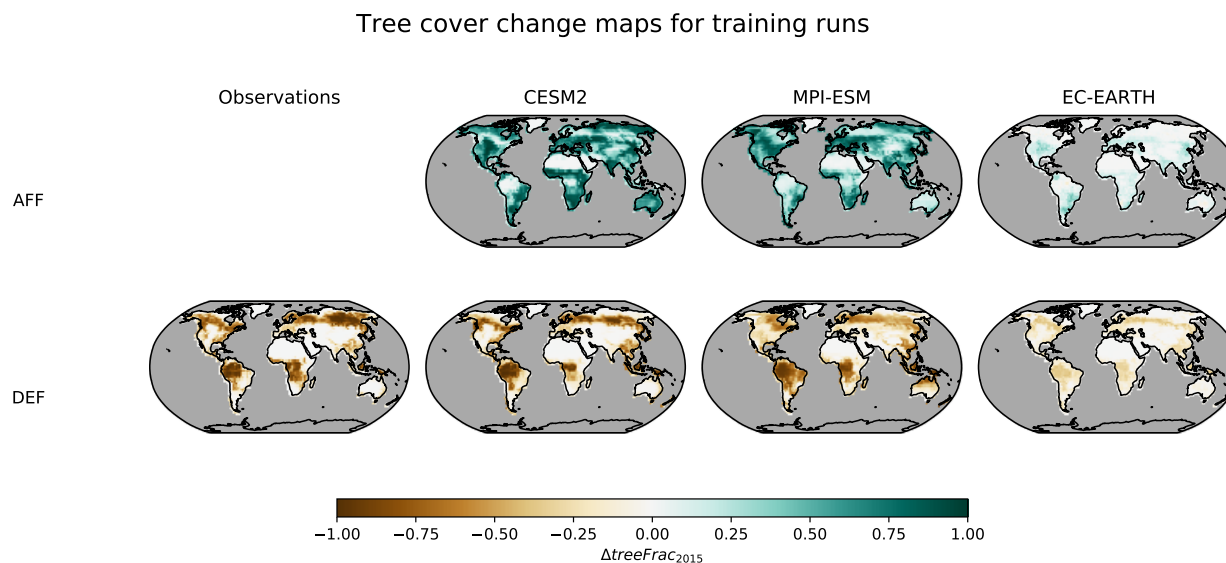


**Figure A1.** Leftmost column shows tree cover change maps for full deforestation relative to the year 2015 as derived by Duveiller et al. (2018b) using observational data. Columns two to four show tree cover change maps relative to the year 2015 implemented in the LAMACLIMA afforestation, AFF (top row), and deforestation, DEF (bottom row), experiments in the CESM2, MPI-ESM and EC-EARTH ESMS.

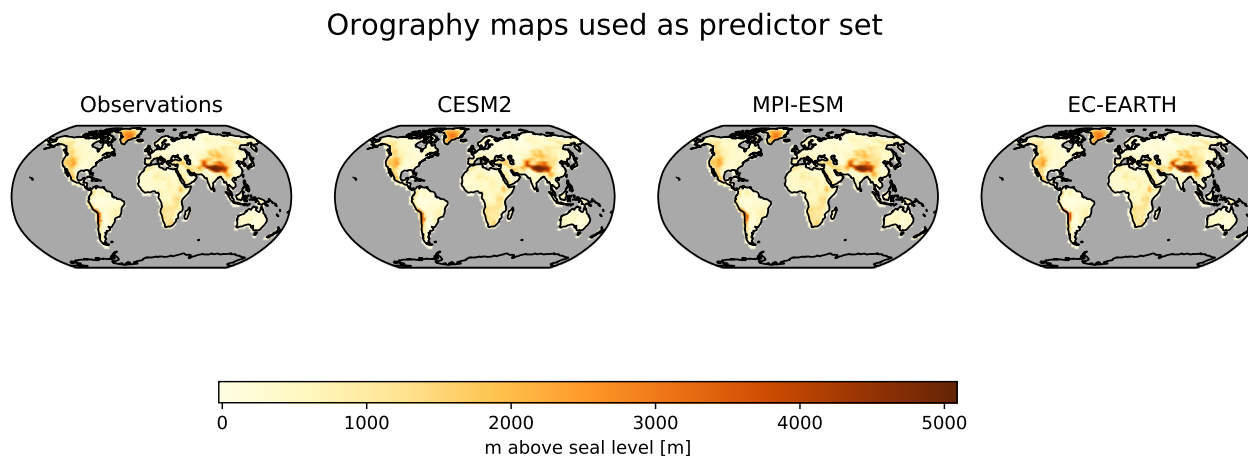


**Figure A2.** Orography features, defined as meters above seal level, used in input predictor matrix for  $\Gamma_m$  for Observations and ESMS (columns).

## Appendix B

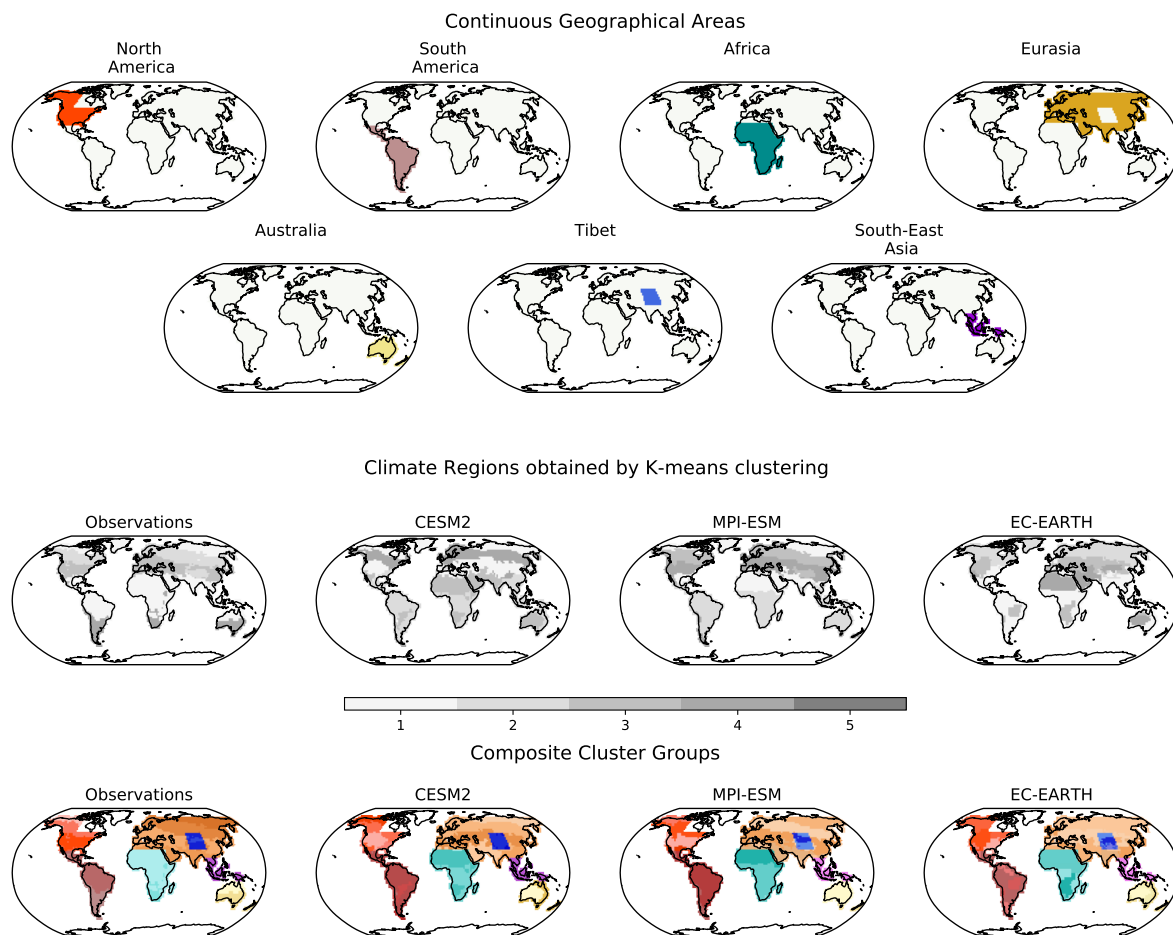


**Figure A1.** Composite cluster blocks obtained by combining clusters of grid points with similar background climate and continuous geographical area. Grid points are clustered into groups with similar background climate using K-means clustering with temperature and relative humidity as indicator variables.

## Appendix B

$TS^{min}$  and  $TS^{max}$  training outputs: CESM2

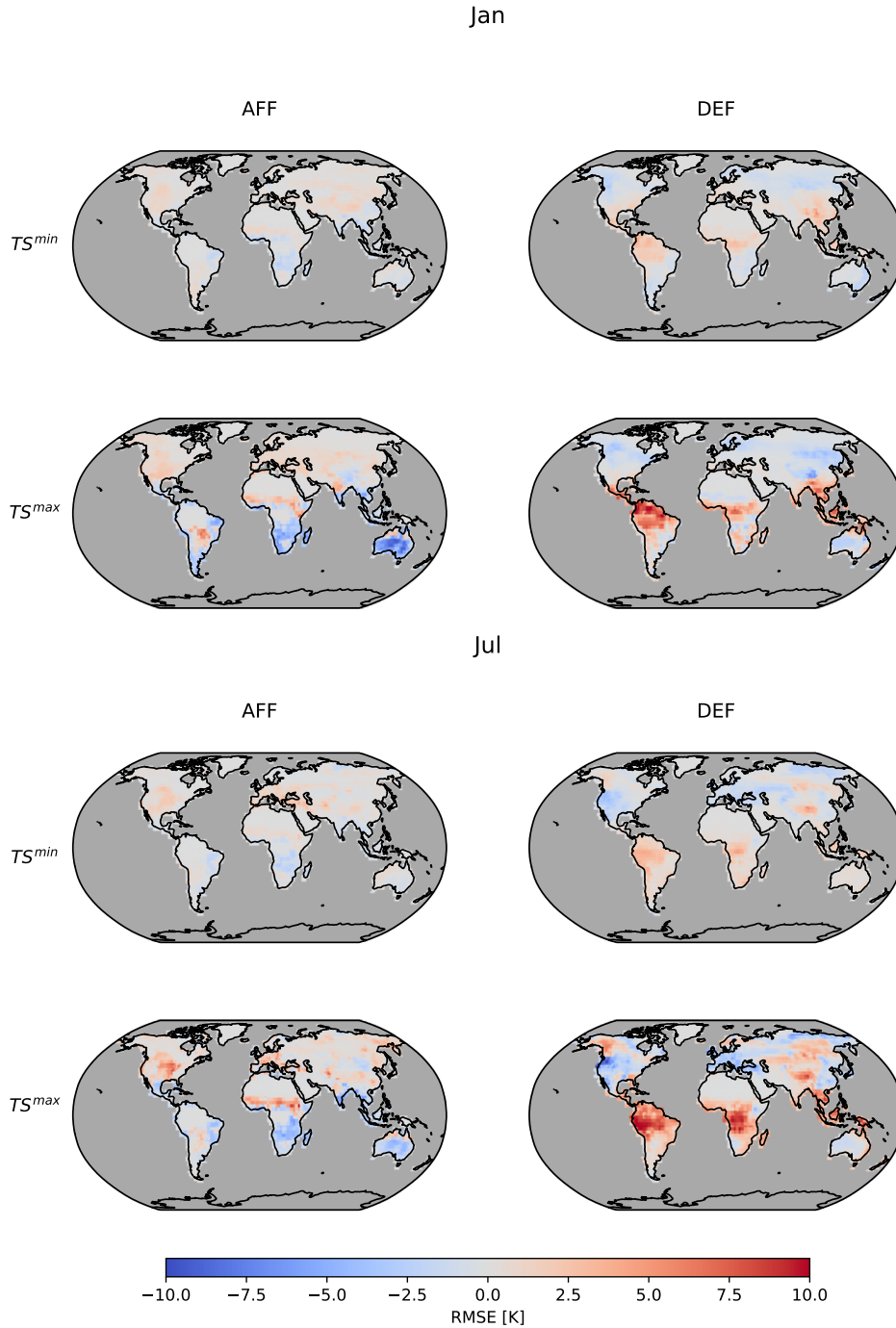


**Figure B1.**  $TS_{m,s}^{min/max}$  responses (rows) from the LAMACLIMA afforestation, AFF, and deforestation, DEF, experiments (columns) for the months of January (upper panel) and July (lower panel)

RMSE of the fully calibrated  $\Gamma_m^{min/max}$  for CESM2

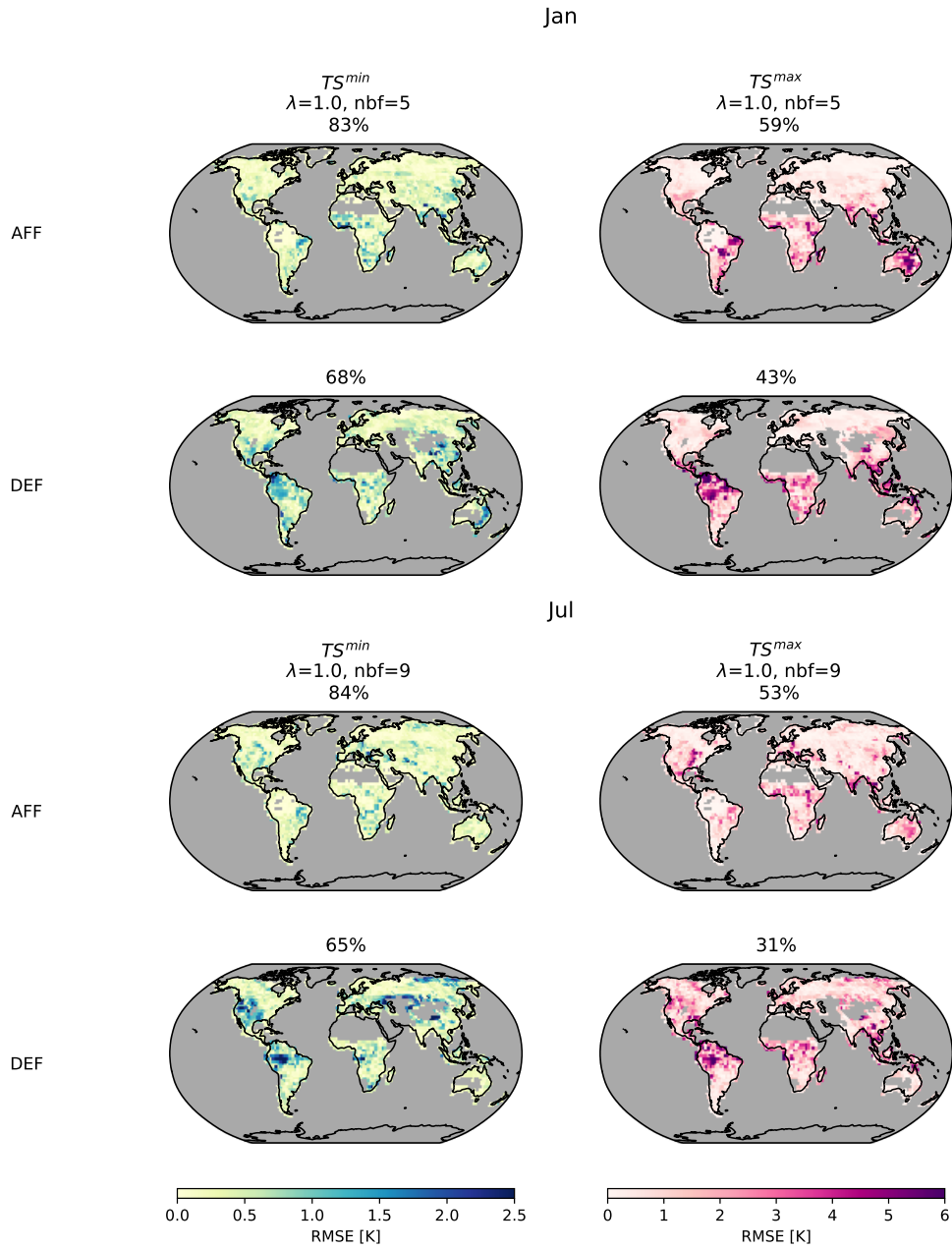


**Figure B2.** Same as Figure 3 but for CESM2,  $TS^{min}$  and  $TS^{max}$

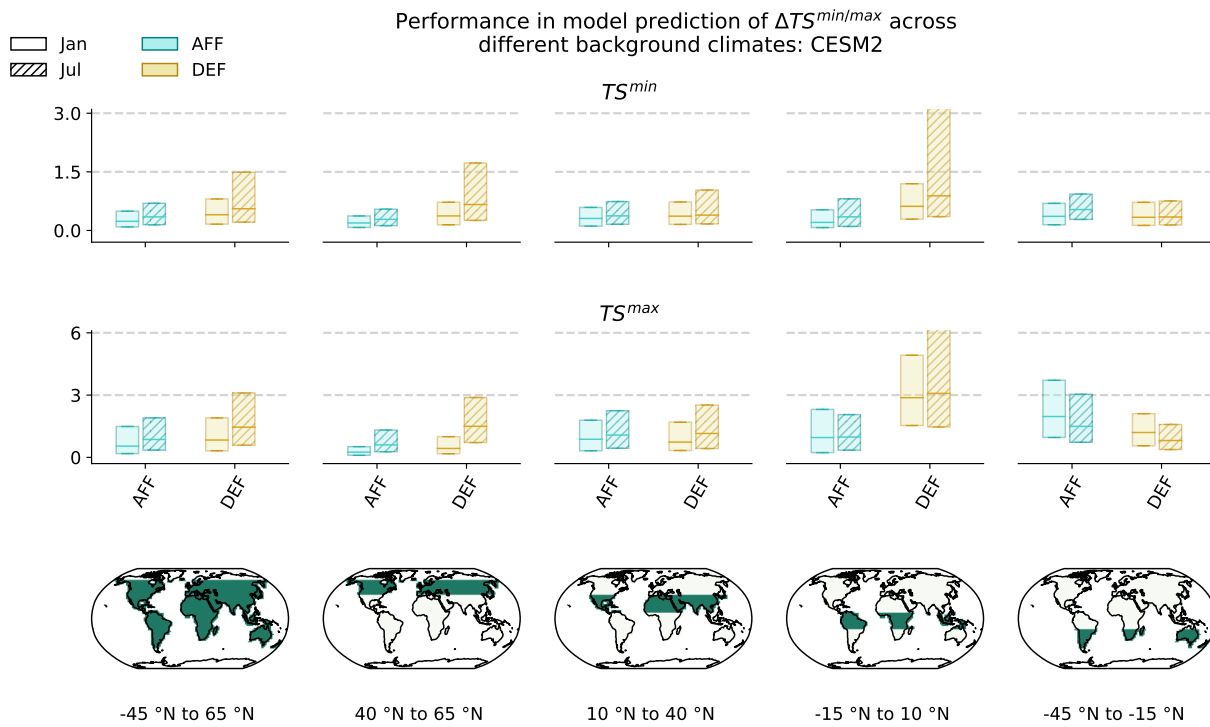


**Figure B3.** Same as Figure 4 but for CESM2,  $TS^{min}$  and  $TS^{max}$

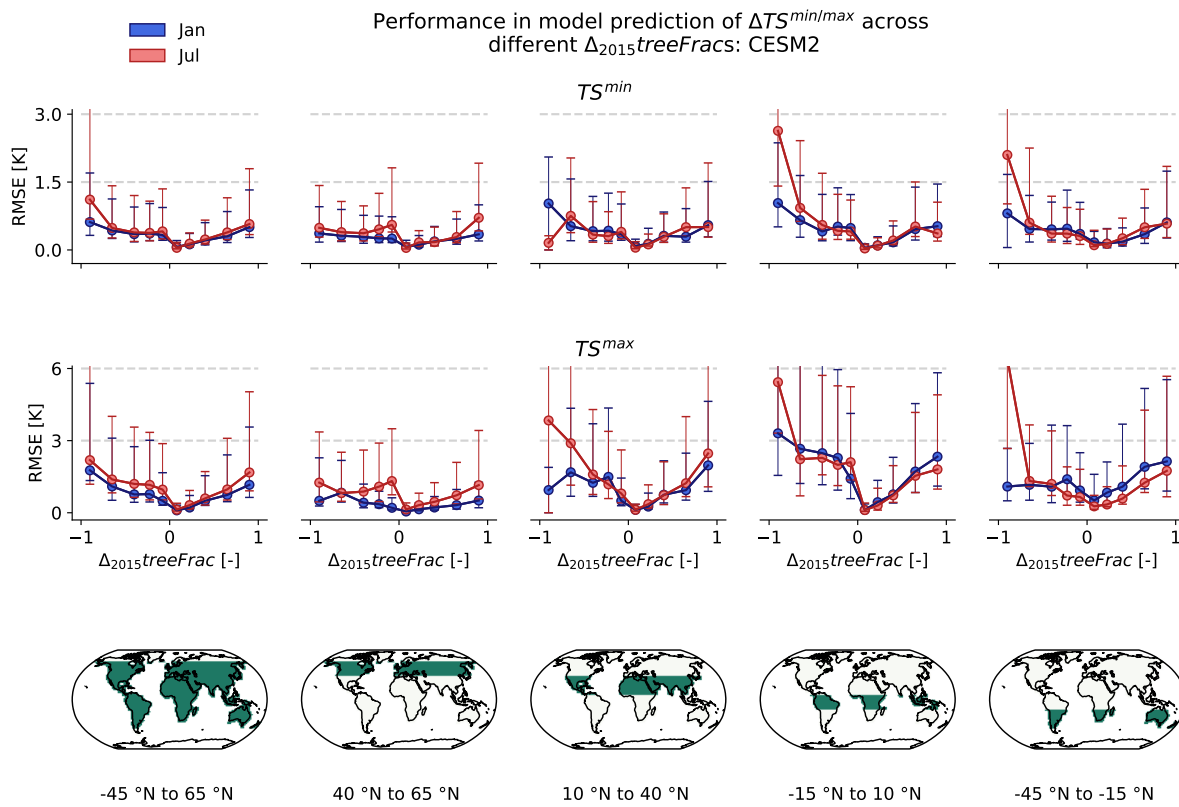


**Figure B4.** Same as Figure 5 but for CESM2,  $TS^{min}$  and  $TS^{max}$

## Appendix C

### Shapiro-Wilk test: Observational MODIS $TS^{night}$ data

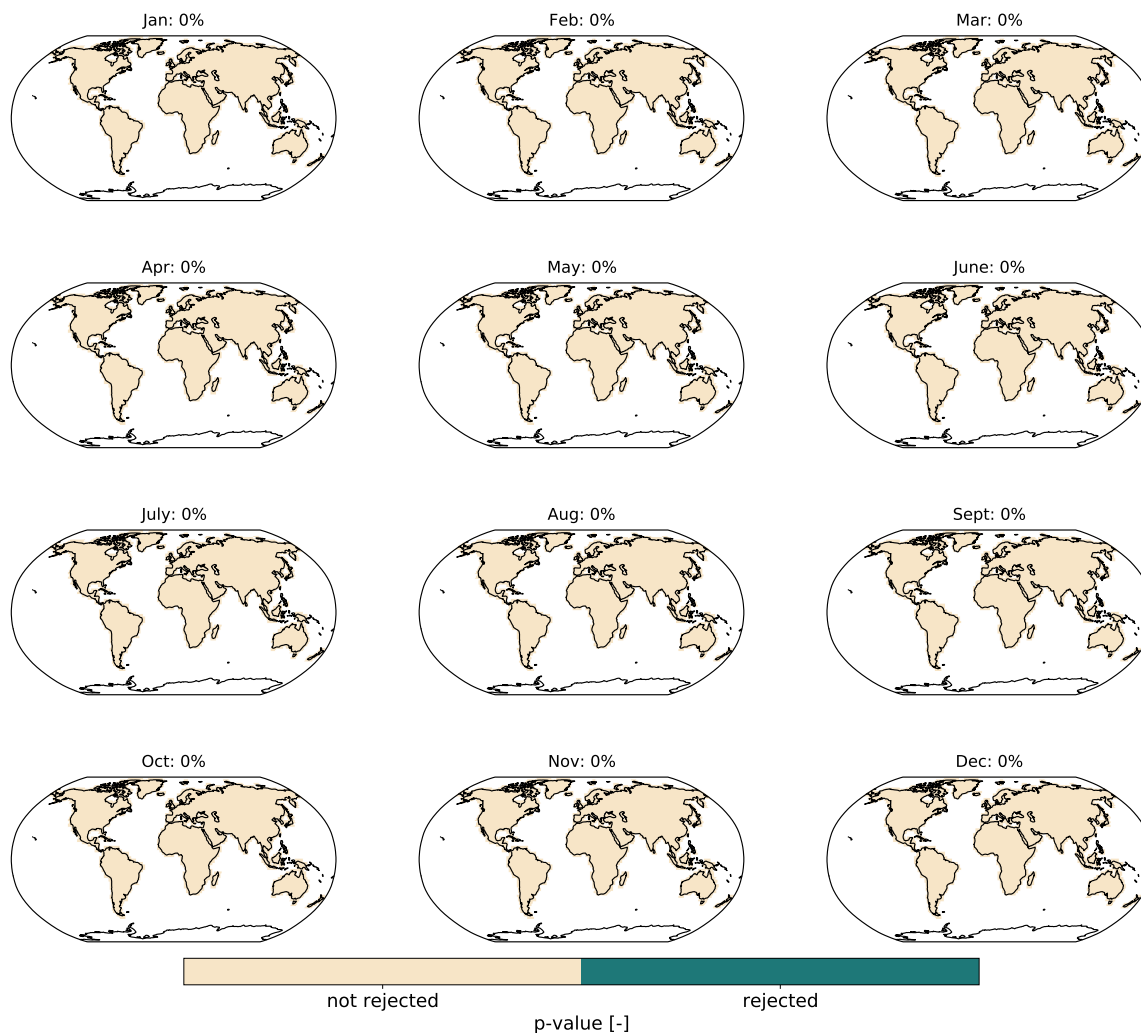


**Figure C1.** Shapiro–Wilk test for normality of  $TS^{night}$  observational data obtained by the MODIS satellite. The null hypothesis is that the residuals are normally distributed. A Benjamini–Hochberg multiple test correction (Benjamini and Hochberg, 1995) is applied to the p values before plotting them. Percentage values indicate the proportion of grid points for which the null hypothesis is rejected.



Shapiro-Wilk test: Observational MODIS  $TS^{day}$  data

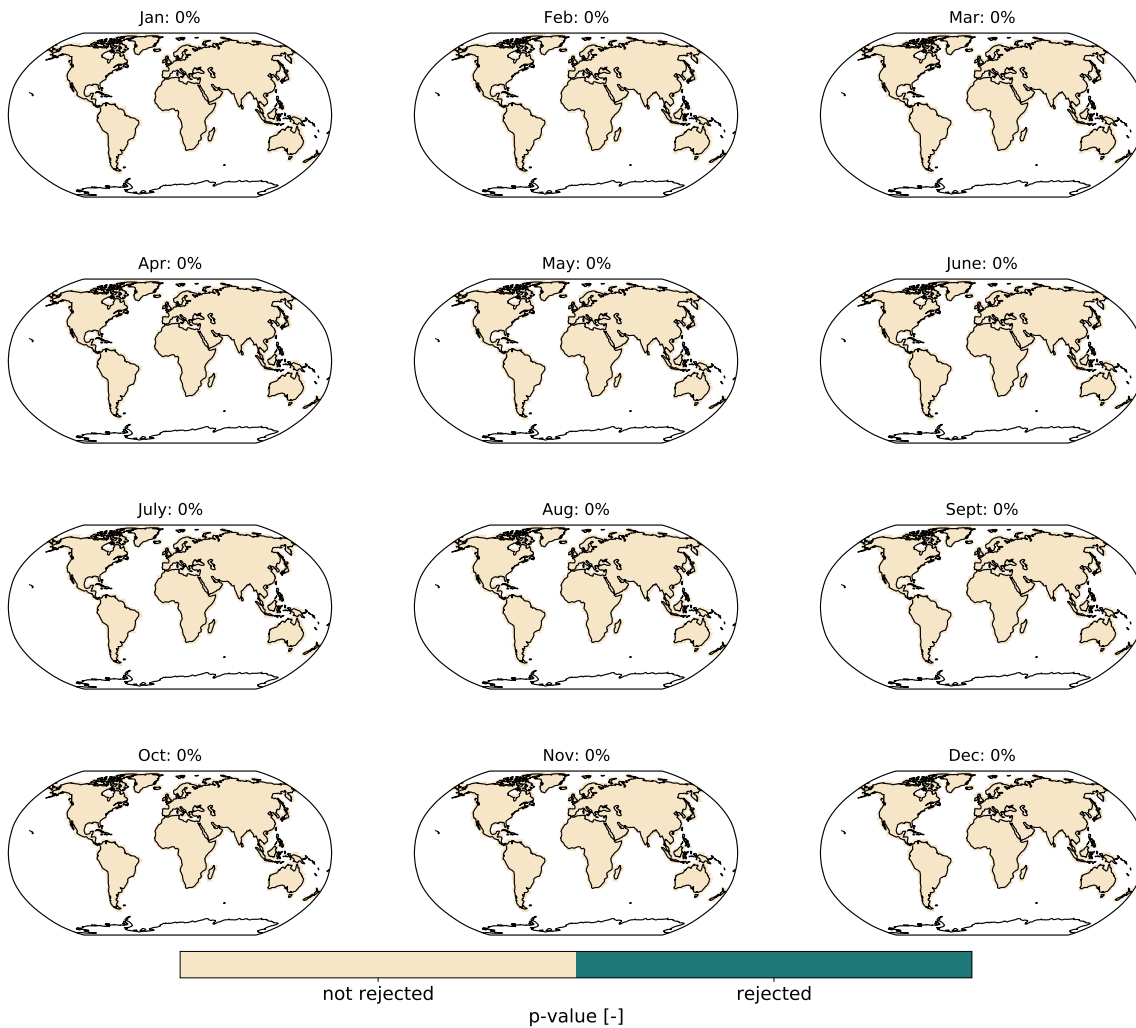


**Figure C2.** Same as Figure C1 but for  $TS^{day}$  observational data obtained by the MODIS satellite

Shapiro-Wilk test: CESM2  $TS^{min}$

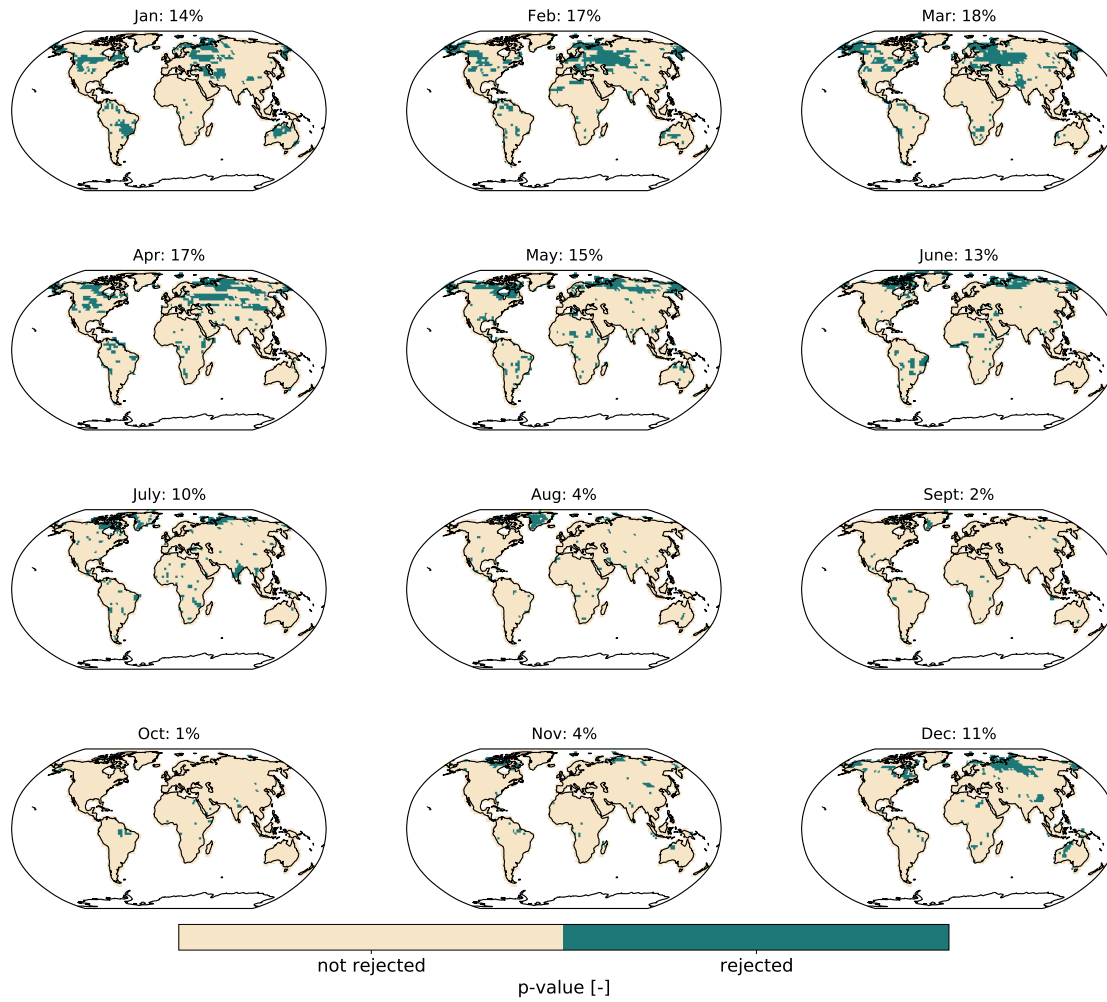


**Figure C3.** Same as Figure C1 but for  $TS^{min}$  data obtained from CESM2

Shapiro-Wilk test: CESM2  $TS^{min}$

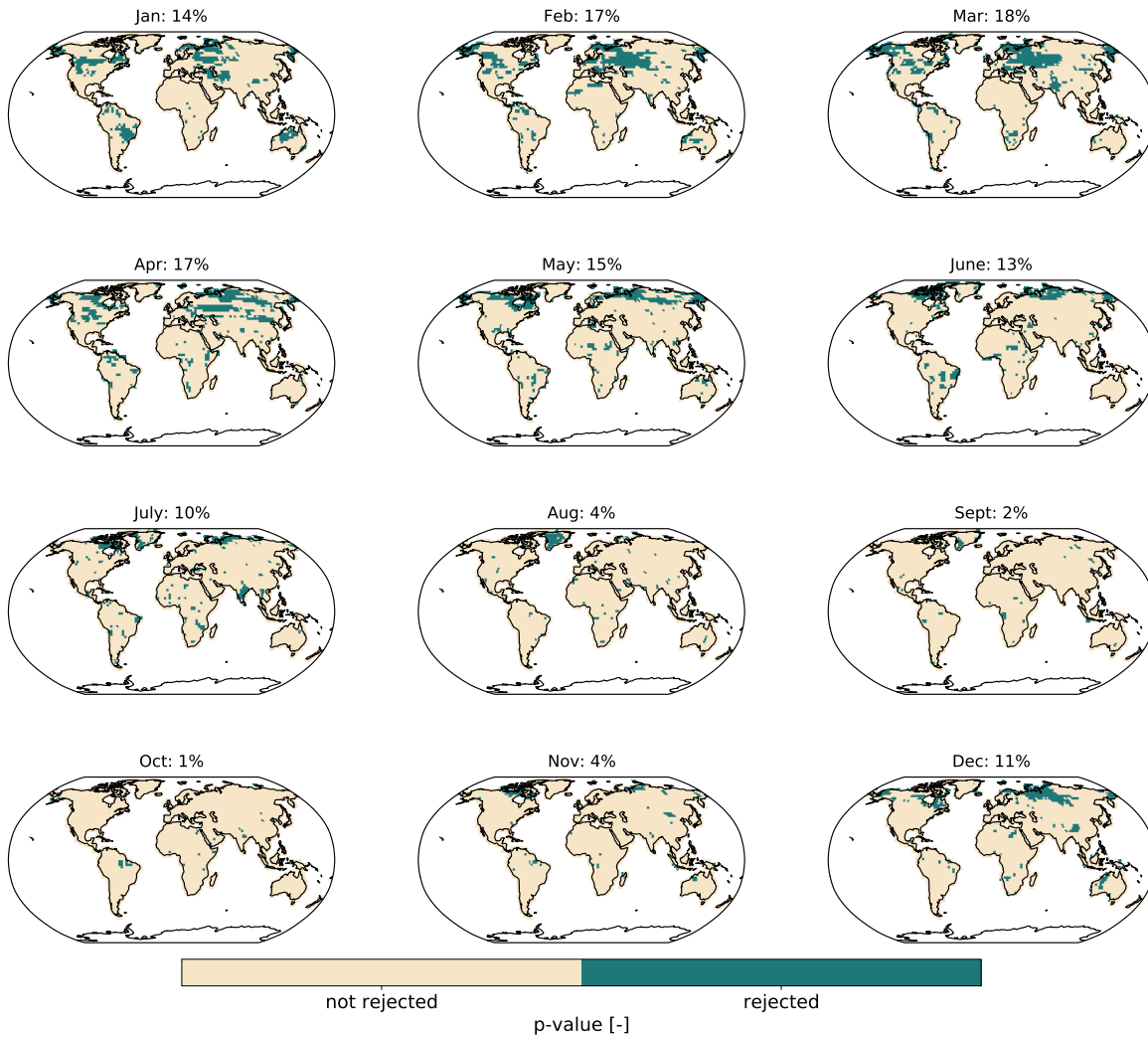


**Figure C4.** Same as Figure C1 but for  $TS^{max}$  data obtained from CESM2

## References

- 620 Glasgow leaders' declaration on forest and land-use, <https://ukcop26.org/glasgow-leaders-declaration-on-forests-and-land-use/>, 2021.
- Alexeeff, S. E., Nychka, D., Sain, S. R., and Tebaldi, C.: Emulating mean patterns and variability of temperature across and within scenarios in anthropogenic climate change experiments, *Climatic Change*, 146, 319–333, <https://doi.org/10.1007/s10584-016-1809-8>, 2018.
- Benjamini, Y. and Hochberg, Y.: benjamini\_hochberg1995, *Journal of the Royal Statistical Society. Series B (Methodological)*, 57, 289–300, <https://www.jstor.org/stable/2346101>, 1995.
- 625 Beusch, L., Gudmundsson, L., and Seneviratne, S. I.: Emulating Earth system model temperatures with MESMER: from global mean temperature trajectories to grid-point-level realizations on land, *Earth System Dynamics*, 11, 139–159, <https://doi.org/10.5194/esd-11-139-2020>, 2020.
- Boisier, J. P., De Noblet-Ducoudré, N., Pitman, A. J., Cruz, F. T., Delire, C., Van Den Hurk, B. J., Van Der Molen, M. K., Miller, C., and Voldoire, A.: Attributing the impacts of land-cover changes in temperate regions on surface temperature and heat fluxes to specific causes: Results from the first LUCID set of simulations, *Journal of Geophysical Research Atmospheres*, 117, 1–16, <https://doi.org/10.1029/2011JD017106>, 2012.
- 630 Boysen, L. R., Brovkin, V., Pongratz, J., Lawrence, D. M., Lawrence, P., Vuichard, N., Peylin, P., Liddicoat, S., Hajima, T., Zhang, Y., Rocher, M., Delire, C., Séférian, R., Arora, V. K., Nieradzik, L., Anthoni, P., Thiery, W., Laguë, M. M., Lawrence, D., and Lo, M. H.: Global climate response to idealized deforestation in CMIP6 models, *Biogeosciences*, 17, 5615–5638, <https://doi.org/10.5194/bg-17-5615-2020>, 2020.
- 635 Brunner, L., Hauser, M., Lorenz, R., and Beyerle, U.: The ETH Zurich CMIP6 next generation archive: technical documentation, <https://doi.org/10.5281/zenodo.3734128>, 2020.
- Calvin, K. and Bond-Lamberty, B.: Integrated human-earth system modeling - State of the science and future directions, *Environmental Research Letters*, 13, <https://doi.org/10.1088/1748-9326/aac642>, 2018.
- Castruccio, S., Hu, Z., Sanderson, B., Karspeck, A., and Hammerling, D.: Reproducing internal variability with few ensemble runs, *Journal of Climate*, 32, 8511–8522, <https://doi.org/10.1175/JCLI-D-19-0280.1>, 2019.
- 640 Davin, E. L., Rechid, D., Breil, M., Cardoso, R. M., Coppola, E., Hoffmann, P., Jach, L. L., Katragkou, E., de Noblet-Ducoudré, N., Radtke, K., Raffa, M., Soares, P. M. M., Sofiadis, G., Strada, S., Strandberg, G., Tölle, M. H., Warrach-Sagi, K., and Wulfmeyer, V.: Biogeophysical impacts of forestation in Europe: first results from the LUCAS (Land Use and Climate Across Scales) regional climate model intercomparison, *Earth System Dynamics*, 11, 183–200, <https://doi.org/10.5194/esd-11-183-2020>, 2020.
- 645 De Hertog, S. J., Havermann, F., Vanderkelen, I., Guo, S., Luo, F., Manola, I., Coumou, D., Davin, E. L., Duveiller, G., Lejeune, Q., Pongratz, J., Schleussner, C.-F., Seneviratne, S. I., and Thiery, W.: The biogeophysical effects of idealized land cover and land management changes in Earth System Models, *Earth System Dynamics Discussions*, pp. 1–53, <https://doi.org/10.5194/esd-2022-5>, 2022.
- De Noblet-Ducoudré, N., Boisier, J. P., Pitman, A., Bonan, G. B., Brovkin, V., Cruz, F., Delire, C., Gayler, V., Van Den Hurk, B. J., Lawrence, P. J., Van Der Molen, M. K., Müller, C., Reick, C. H., Strengers, B. J., and Voldoire, A.: Determining robust impacts of land-use-induced land cover changes on surface climate over North America and Eurasia: Results from the first set of LUCID experiments, *Journal of Climate*, 25, 3261–3281, <https://doi.org/10.1175/JCLI-D-11-00338.1>, 2012.
- 650 Duveiller, G., Forzieri, G., Robertson, E., Li, W., Georgievski, G., Lawrence, P., Wiltshire, A., Ciais, P., Pongratz, J., Sitch, S., Arneth, A., and Cescatti, A.: Biophysics and vegetation cover change: A process-based evaluation framework for confronting land surface models with satellite observations, *Earth System Science Data*, 10, 1265–1279, <https://doi.org/10.5194/essd-10-1265-2018>, 2018a.

- 655 Duveiller, G., Hooker, J., and Cescatti, A.: The mark of vegetation change on Earth's surface energy balance, *Nature Communications*, 9, <https://doi.org/10.1038/s41467-017-02810-8>, 2018b.
- Duveiller, G., Hooker, J., and Cescatti, A.: A dataset mapping the potential biophysical effects of vegetation cover change, *Scientific Data*, 5, 1–15, <https://doi.org/10.1038/sdata.2018.14>, 2018c.
- Duveiller, G., Hooker, J., and Cescatti, A.: A dataset mapping the potential biophysical effects of vegetation cover change. figshare, 660 <https://doi.org/https://doi.org/10.6084/m9.figshare.c.3829333.v1>, 2018d.
- Efron, B. and Tibshirani, R. J.: *An Introduction to the Bootstrap*, <https://doi.org/10.1007/978-1-4899-4541-9>, 1993.
- Fujimori, S., Hasegawa, T., Masui, T., Takahashi, K., Herran, D. S., Dai, H., Hijikawa, Y., and Kainuma, M.: SSP3: AIM implementation of Shared Socioeconomic Pathways, *Global Environmental Change*, 42, 268–283, <https://doi.org/10.1016/j.gloenvcha.2016.06.009>, 2017.
- Hastie, T. and Tibshirani, R.: Generalized additive models, *Statistical Science*, 1, 297–318, 1986.
- 665 Hastie, T. and Tibshirani, R.: Varying Coefficients Model, *Journal of the Royal Statistical Society. Series B (Methodological)*, 55, 757–796, 1993.
- Hirsch, A. L., Guillod, B. P., Seneviratne, S. I., Beyerle, U., Boysen, L. R., Brovkin, V., Davin, E. L., Doelman, J. C., Kim, H., Mitchell, D. M., Nitta, T., Shiogama, H., Sparrow, S., Stehfest, E., van Vuuren, D. P., and Wilson, S.: Biogeophysical Impacts of Land-Use Change on Climate Extremes in Low-Emission Scenarios: Results From HAPPI-Land, *Earth's Future*, 6, 396–409, 670 <https://doi.org/10.1002/2017EF000744>, 2018.
- Hooker, J., Duveiller, G., and Cescatti, A.: Data descriptor: A global dataset of air temperature derived from satellite remote sensing and weather stations, *Scientific Data*, 5, 1–11, <https://doi.org/10.1038/sdata.2018.246>, 2018.
- Lawrence, D., Coe, M., Walker, W., Verchot, L., and Vandecar, K.: The Unseen Effects of Deforestation: Biophysical Effects on Climate, *Frontiers in Forests and Global Change*, 5, 1–13, <https://doi.org/10.3389/ffgc.2022.756115>, 2022.
- 675 Lawrence, D. M., Hurtt, G. C., Arneth, A., Brovkin, V., Calvin, K. V., Jones, A. D., Jones, C. D., Lawrence, P. J., Noblet-Ducoudré, N. D., Pongratz, J., Seneviratne, S. I., and Shevliakova, E.: The Land Use Model Intercomparison Project (LUMIP) contribution to CMIP6: Rationale and experimental design, *Geoscientific Model Development*, 9, 2973–2998, <https://doi.org/10.5194/gmd-9-2973-2016>, 2016.
- Lejeune, Q., Davin, E. L., Gudmundsson, L., Winckler, J., and Seneviratne, S. I.: Historical deforestation locally increased the intensity of hot days in northern mid-latitudes, *Nature Climate Change*, 8, 386–390, <https://doi.org/10.1038/s41558-018-0131-z>, 2018.
- 680 Li, Y., Zhao, M., Motesharrei, S., Mu, Q., Kalnay, E., and Li, S.: Local cooling and warming effects of forests based on satellite observations, *Nature Communications*, 6, 6603, <https://doi.org/10.1038/ncomms7603>, 2015.
- Link, R., Snyder, A., Lynch, C., Hartin, C., Kravitz, B., and Bond-Lamberty, B.: Fldgen v1.0: An emulator with internal variability and space-Time correlation for Earth system models, *Geoscientific Model Development*, 12, 1477–1489, <https://doi.org/10.5194/gmd-12-1477-2019>, 2019.
- 685 Liu, G., Peng, S., Huntingford, C., and Xi, Y.: A new precipitation emulator (PREMU v1.0) for lower complexity models, 2022.
- Luysaert, S., Jammot, M., Stoy, P. C., Estel, S., Pongratz, J., Ceschia, E., Churkina, G., Don, A., Erb, K., Ferlicoq, M., Gielen, B., Grünwald, T., Houghton, R. A., Klumpp, K., Knohl, A., Kolb, T., Kuemmerle, T., Laurila, T., Lohila, A., Loustau, D., McGrath, M. J., Meyfroidt, P., Moors, E. J., Naudts, K., Novick, K., Otto, J., Pilegaard, K., Pio, C. A., Rambal, S., Reibmann, C., Ryder, J., Suyker, A. E., Varlagin, A., Wattenbach, M., and Dolman, A. J.: Land management and land-cover change have impacts of similar magnitude on surface temperature, 690 *Nature Climate Change*, 4, 389–393, <https://doi.org/10.1038/nclimate2196>, 2014.
- McKinnon, K. A. and Deser, C.: Internal variability and regional climate trends in an observational large ensemble, *Journal of Climate*, 31, 6783–6802, <https://doi.org/10.1175/JCLI-D-17-0901.1>, 2018.

- Meier, R., Davin, E. L., Lejeune, Q., Hauser, M., Li, Y., Martens, B., Schultz, N. M., Sterling, S., and Thiery, W.: Evaluating and improving the Community Land Model's sensitivity to land cover, *Biogeosciences*, 15, 4731–4757, <https://doi.org/10.5194/bg-15-4731-2018>, 2018.
- 695 Menne, M. J., Williams, C. N., Gleason, B. E., Rennie, J. J., and Lawrimore, J. H.: The Global Historical Climatology Network Monthly Temperature Dataset, Version 4, *Journal of Climate*, 31, 9835–9854, <https://doi.org/10.1175/JCLI-D-18-0094.1>, 2018.
- Nath, S.: snath-xoc/TIMBER-v0.1\_Nath\_et\_al\_2022: TIMBER, <https://doi.org/10.5281/zenodo.7261281>, 2022.
- Nath, S., Hertog, S. J. D., Guo, S., Havermann, F., Luo, F., Manola, I., Pongratz, J., and Thiery, W.: LAMACLIMA\_experiments\_for\_training\_TIMBERv0.1, <https://doi.org/10.5281/zenodo.7261374>, 2022a.
- 700 Nath, S., Lejeune, Q., Beusch, L., Seneviratne, S. I., and Schleussner, C. F.: MESMER-M: an Earth system model emulator for spatially resolved monthly temperature, *Earth System Dynamics*, 13, 851–877, <https://doi.org/10.5194/esd-13-851-2022>, 2022b.
- Pitman, A., De Noblet-Ducoudré, N., Avila, F., Alexander, L., Boisier, J.-P., Brovkin, V., Delire, C., Cruz, F., Donat, M., Gayler, V., Hurk, B. v. d., Reick, C., and Voldoire, A.: Effects of land cover change on temperature and rainfall extremes in multi-model ensemble 3 simulations, *Earth System Dynamics*, p. 213–231, 2012.
- 705 Popp, A., Calvin, K., Fujimori, S., Havlik, P., Humpenöder, F., Stehfest, E., Bodirsky, B. L., Dietrich, J. P., Doelman, J. C., Gusti, M., Hasegawa, T., Kyle, P., Obersteiner, M., Tabeau, A., Takahashi, K., Valin, H., Waldhoff, S., Weindl, I., Wise, M., Kriegler, E., Lotze-Campen, H., Fricko, O., Riahi, K., and Vuuren, D. P.: Land-use futures in the shared socio-economic pathways, *Global Environmental Change*, 42, 331–345, <https://doi.org/10.1016/j.gloenvcha.2016.10.002>, 2017.
- Quilcaille, Y., Gudmundsson, L., Beusch, L., Hauser, M., and Seneviratne, S. I.: Showcasing MESMER-X: Spatially resolved emulation of annual maximum temperatures of Earth System Models, pp. 1–11, <https://doi.org/10.1029/2022GL099012>, 2022.
- 710 Riahi, K., van Vuuren, D. P., Kriegler, E., Edmonds, J., O'Neill, B. C., Fujimori, S., Bauer, N., Calvin, K., Dellink, R., Fricko, O., Lutz, W., Popp, A., Cuaresma, J. C., KC, S., Leimbach, M., Jiang, L., Kram, T., Rao, S., Emmerling, J., Ebi, K., Hasegawa, T., Havlik, P., Humpenöder, F., Da Silva, L. A., Smith, S., Stehfest, E., Bosetti, V., Eom, J., Gernaat, D., Masui, T., Rogelj, J., Strefler, J., Drouet, L., Krey, V., Luderer, G., Harmsen, M., Takahashi, K., Baumstark, L., Doelman, J. C., Kainuma, M., Klimont, Z., Marangoni, G., Lotze-Campen, H., Obersteiner, M., Tabeau, A., and Tavoni, M.: The Shared Socioeconomic Pathways and their energy, land use, and greenhouse gas emissions implications: An overview, *Global Environmental Change*, 42, 153–168, <https://doi.org/10.1016/j.gloenvcha.2016.05.009>, 2017.
- 715 Roberts, D. R., Bahn, V., Ciuti, S., Boyce, M. S., Elith, J., Guillera-Arroita, G., Hauenstein, S., Lahoz-Monfort, J. J., Schröder, B., Thuiller, W., Warton, D. I., Wintle, B. A., Hartig, F., and Dormann, C. F.: Cross-validation strategies for data with temporal, spatial, hierarchical, or phylogenetic structure, *Ecography*, 40, 913–929, <https://doi.org/10.1111/ecog.02881>, 2017.
- Seddon, N., Sengupta, S., Hauler, I., and Rizvi, A. R.: Nature-based solutions in nationally determined contributions | IUCN Library System, <https://portals.iucn.org/library/node/48525>, 2020.
- Seneviratne, S. I., Wartenburger, R., Guillod, B. P., Hirsch, A. L., Vogel, M. M., Brovkin, V., Van Vuuren, D. P., Schaller, N., Boysen, L., Calvin, K. V., Doelman, J., Greve, P., Havlik, P., Humpenöder, F., Krisztin, T., Mitchell, D., Popp, A., Riahi, K., Rogelj, J., Schleussner, C. F., Sillmann, J., and Stehfest, E.: Climate extremes, land-climate feedbacks and land-use forcing at 1.5C, *Philosophical Transactions of the Royal Society A: Mathematical, Physical and Engineering Sciences*, 376, <https://doi.org/10.1098/rsta.2016.0450>, 2018.
- 725 Thiery, W., Davin, E. L., Lawrence, D. M., Hirsch, A. L., Hauser, M., and Seneviratne, S. I.: Present-day irrigation mitigates heat extremes, *Journal of Geophysical Research*, 122, 1403–1422, <https://doi.org/10.1002/2016JD025740>, 2017.

- Thiery, W., Visser, A. J., Fischer, E. M., Hauser, M., Hirsch, A. L., Lawrence, D. M., Lejeune, Q., Davin, E. L., and Seneviratne, S. I.:  
730 Warming of hot extremes alleviated by expanding irrigation, *Nature Communications*, 11, 290, <https://doi.org/10.1038/s41467-019-14075-4>, 2020.
- Van Vuuren, D. P., Battle Bayer, L., Chuwah, C., Ganzeveld, L., Hazeleger, W., Van Den Hurk, B., Van Noije, T., Oneill, B., and Strengers, B. J.: A comprehensive view on climate change: Coupling of earth system and integrated assessment models, *Environmental Research Letters*, 7, <https://doi.org/10.1088/1748-9326/7/2/024012>, 2012.
- 735 van Vuuren, D. P., Stehfest, E., Gernaat, D. E., Doelman, J. C., van den Berg, M., Harmsen, M., de Boer, H. S., Bouwman, L. F., Daioglou, V., Edelenbosch, O. Y., Girod, B., Kram, T., Lassaletta, L., Lucas, P. L., van Meijl, H., Müller, C., van Ruijven, B. J., van der Sluis, S., and Tabeau, A.: Energy, land-use and greenhouse gas emissions trajectories under a green growth paradigm, *Global Environmental Change*, 42, 237–250, <https://doi.org/10.1016/j.gloenvcha.2016.05.008>, 2017.
- Winckler, J., Reick, C. H., and Pongratz, J.: Robust identification of local biogeophysical effects of land-cover change in a global climate  
740 model, *Journal of Climate*, 30, 1159–1176, <https://doi.org/10.1175/JCLI-D-16-0067.1>, 2017a.
- Winckler, J., Reick, C. H., and Pongratz, J.: Why does the locally induced temperature response to land cover change differ across scenarios?, *Geophysical Research Letters*, 44, 3833–3840, <https://doi.org/10.1002/2017GL072519>, 2017b.
- Winckler, J., Reick, C. H., and Pongratz, J.: Robust identification of local biogeophysical effects of land-cover change in a global climate  
model, *Journal of Climate*, 30, 1159–1176, <https://doi.org/10.1175/JCLI-D-16-0067.1>, 2017c.
- 745 Windisch, M. G., Davin, E. L., and Seneviratne, S. I.: Prioritizing forestation based on biogeochemical and local biogeophysical impacts, *Nature Climate Change*, 11, 867–871, <https://doi.org/10.1038/s41558-021-01161-z>, 2021.
- Wood, S. N.: *Generalized Additive Models*, Chapman and Hall/CRC, <https://doi.org/10.1201/9781315370279>, 2017.
- Yee, T. W. and Stephenson, A. G.: Vector generalized linear and additive extreme value models, *Extremes*, 10, 1–19, <https://doi.org/10.1007/s10687-007-0032-4>, 2007.